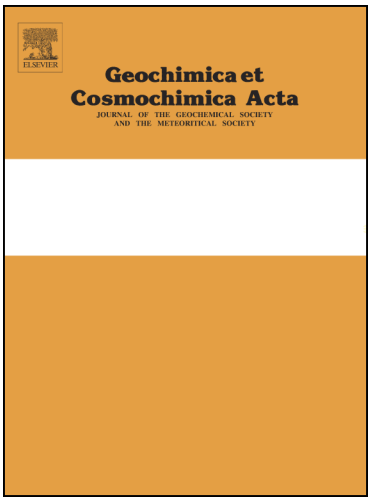

Seconds after impact: Insights into the thermal history of impact ejecta from diffusion between lechatelierite and host glass in tektites and experiments

Catherine A. Macris, Paul D. Asimow, James Badro, John M. Eiler, Youxue Zhang, Edward M. Stolper

PII: S0016-7037(18)30475-7
DOI: https://doi.org/10.1016/j.gca.2018.08.031
Reference: GCA 10904

To appear in: *Geochimica et Cosmochimica Acta*

Received Date: 29 March 2017
Revised Date: 15 August 2018
Accepted Date: 17 August 2018

Please cite this article as: Macris, C.A., Asimow, P.D., Badro, J., Eiler, J.M., Zhang, Y., Stolper, E.M., Seconds after impact: Insights into the thermal history of impact ejecta from diffusion between lechatelierite and host glass in tektites and experiments, *Geochimica et Cosmochimica Acta* (2018), doi: https://doi.org/10.1016/j.gca.2018.08.031

Seconds after impact: Insights into the thermal history of impact ejecta from diffusion between lechatelierite and host glass in tektites and experiments

Catherine A. Macris[1*], Paul D. Asimow[1], James Badro[2], John M. Eiler[1], Youxue Zhang[3], and Edward M. Stolper[1]

[1]Division of Geological and Planetary Sciences, California Institute of Technology, Pasadena, CA, 91125, USA.

[2]Institut de Physique du Globe de Paris, Paris, France.

[3]Earth and Environmental Sciences, University of Michigan, Ann Arbor, MI, 48109, USA.

*Corresponding Author. Current affiliation: Department of Earth Sciences, Indiana University – Purdue University Indianapolis, Indianapolis, IN, 46202, USA.

Correspondent email address: camacris@iupui.edu

1 ABSTRACT

Tektites contain inclusions of lechatelierite, nearly pure SiO_2 glass formed by quenching of quartz grains melted during hypervelocity impacts. We report the discovery in a tektite of chemically zoned boundary layers (ca 20 μm) between lechatelierite and host felsic glass. These boundary layers in tektites formed by chemical diffusion between molten silica inclusions (quenched to lechatelierite on cooling) and surrounding felsic melt. We reproduced the details of these boundary layers via experiments on mixtures of powdered natural tektite plus quartz grains heated to 1800-2400 ˚C for 1-120 s using an aerodynamic levitation laser heating furnace. The results of these experiments were used to provide quantitative constraints on possible thermal histories of the natural sample.

The experiments successfully reproduced all major aspects of the concentration profiles from the natural sample including diffusion length scale, strong asymmetry of the concentration profiles with respect to the Matano plane (due to the strong concentration dependence of the diffusivities of all oxides on SiO_2 content), similarities in lengths of the diffusive profiles (due to control by the diffusion of SiO_2 on the diffusivity of the other oxides), and differences in the shapes of the profiles among the oxides (including a maximum in the diffusion profile of K_2O due to uphill diffusion). The characteristic lengths of all non-alkali oxide profiles are proportional to $\sqrt{t}$ from which diffusivities and activation energies can be derived; these results are consistent with measurements in melts with lower SiO_2 contents and at lower temperatures reported in the literature. We also fit the experimental profiles of SiO_2 and Al_2O_3 using simple formulations of the dependence of their diffusivities on SiO_2 content and temperature, yielding results similar to those obtained from the $\sqrt{t}$ dependence of the characteristic profile lengths.

The quantitative characterization of diffusion in boundary layers based on our experiments allow us to set limits on the thermal history of the natural tektite in which the boundary layers were discovered. If the interdiffusion between the silica and felsic melts occurred at constant temperature, the duration of heating experienced by the natural tektite we studied depends on temperature; possible solutions include heating at ~2000 °C for ~70 s, -2400 °C for ~3 seconds. We also explored non-isothermal, asymptotic cooling histories; for a maximum temperature of 2400 °C, a characteristic cooling time scale of ~50 s is implied, whereas, for 2000 °C, the time scale is ~1400 s. Further, a maximum temperature of ~2360 °C yields an effective diffusive time scale of ~5 s, a cooling time scale of ~90 s, and a cooling rate at the glass transition temperature of ~5 °C/s; results that are consistent with independent estimates of cooling time scales for ~1 cm clasts (Xu and Zhang, 2002), as well as cooling rates at the glass transition temperature (Wilding et al., 1996) – thus satisfying all currently available relevant data. More complex *T-t* paths are possible and can also be modeled using our experimental results and compared with and used as tests of the accuracy of physical models of tektite-forming impact events.

2 INTRODUCTION

Impact processes have had significant effects on rocky bodies in the solar system. On Earth these include effects on the geological record, the environment, and life (e.g., Ahrens and O'Keefe, 1972; Grieve, 1980; Grieve, 1987; Melosh, 1989; Simonson and Glass, 2004; Osinski and Pierazzo, 2012). Although theories of impact processes are sophisticated and useful (e.g., Melosh, 1989), our understanding of the properties and histories of specific impact events is incomplete. This paper focuses on tektites, which are natural terrestrial impact glasses, the origin of which (although at one time controversial, e.g., O'Keefe, 1976; King, 1977; Glass, 1990) is now attributed to melting and quenching of distally ejected target material upon hypervelocity

(>11 km/s) impacts on Earth (e.g., Barnes, 1940; Barnes, 1964; Glass, 1990; Koeberl, 1990; Koeberl, 1994; Artemieva, 2002; Stöffler et al., 2002; Howard, 2011; Osinski et al., 2012; Johnson and Melosh, 2014). The goal of the work described in this paper is to develop quantitative constraints on the thermal histories of tektites that can be used to test and guide models of the impacts that produced them.

Tektites are usually rounded, black or brown, less commonly green, or rarely grey (Koeberl, 1986; Osinski et al., 2012), glassy objects of felsic composition that range in size from submillimeter (microtektites) to tens of centimeters. Tektites are grouped into three categories: (1) splash-form tektites (Fig. 1a), which are the most common and have shapes that suggest they solidified from rotating melts (teardrops, dumbbells, ellipsoids, etc.); (2) aerodynamically shaped tektites, which show signs of atmospheric ablation in their final morphology (flanged buttons); and (3) Muong-Nong type (also called layered tektites), which are the largest tektites and usually have a blocky external shape with a layered internal structure (e.g., Glass, 1990; Koeberl, 1992; Osinski et al., 2012). Even though over 190 impact structures have been identified on Earth (http://www.passc.net/EarthImpactDatabase/index.html), there are currently only four recognized tektite strewn fields around the world: the North American, Central European, Ivory Coast, and Australasian strewn fields (e.g., Glass, 1990). The Australasian strewn field is the youngest (0.77 Ma), the largest (~50,000,000 km^2), and the only one for which an impact crater has not yet been identified (e.g., Glass, 1990; Koeberl, 1992).

It is unclear why so few impact craters are associated with tektites. The record of young impact craters, in particular, is good enough that preservation bias cannot be a complete explanation. The fundamentals of the formation of impact cratering are generally well understood and canonically described in three non-discrete stages that are dominated by different physical processes (Melosh, 1989; Collins et al., 2012). The first stage, 'contact and compression', requires a projectile of sufficient size to arrive at hypervelocity and collide with the target's surface, resulting in shock waves that propagate through both the projectile and target material. The impactor is decelerated, compressed, and heated as it pushes the target

material out of its path. Melting or vaporization of both the projectile and upper layers of target material may occur upon unloading from shock pressures. Following unloading of the projectile from high pressure, the second stage, 'excavation', begins. During excavation, a shock wave continues to propagate through the target, followed by rarefaction, which sets the target material in motion, thereby excavating and opening the crater. After the crater is fully excavated, the third stage, 'modification', produces an intermediate, bowl-shape crater, that generally collapses to form the final crater geometry which may vary.

While the processes of crater formation described above have been the subject of intense research (e.g., Gault et al., 1968; Melosh, 1989; O'Keefe and Ahrens, 1993; Stöffler and Langenhorst, 1994; French, 1998), the particular conditions that lead to effective melt production from the upper layer of the target and therefore to tektite formation, which may include such factors as the composition of the impactor and target material, angle of impact, and the presence or absence of water, are still not well constrained (Artemieva, 2002). There is consensus in the literature as to the general mechanism of tektite formation in which a plume of molten and vaporized material from the target and projectile are ejected from the impact site during the very earliest stages of excavation of the transient crater (e.g., Melosh, 1989; Koeberl, 1994; Howard, 2011). This highly pressurized vapor plume expands out of the growing crater in a powerful wave that pushes away the ambient atmosphere in its path, allowing ejected melt to follow long ballistic trajectories while entrained in the hot vapor (e.g., Melosh, 1989; Howard, 2011). At some later time the melt cools mid-flight, quickly enough to vitrify, and falls back to Earth. Numerical models of tektite formation, evolution, and spatial distribution suggest that production of tektites on Earth requires intermediate angle (between 30-50° from horizontal) hypervelocity impacts into silica-rich targets (Artemieva, 2002; Stöffler et al., 2002; Osinski et al., 2012). In the following two paragraphs we summarize the results of Stöffler et al. (2002) as an example of an effort to quantify the conditions achieved during such an impact.

Stöffler et al. (2002) present a numerical model for a Ries-type impact event, associated with the production of moldavites, which are tektites of the Central European strewn field dated at

~15 Ma. This hydrocode simulation is of a 30° (angle from surface of target), 20 km/s impact of a 1.5 km diameter asteroid (density = 2.5 g/cm^3) into a layered target consisting of loose quartz sand overlying limestone, sandstone, and crystalline basement. According to the simulation, the uppermost sand layer at the impact site (i.e., the tektite parent material) was melted and vaporized, ejected from the crater, and disrupted into particles within four seconds of initial impact. Ejection of molten and solid material from deeper target layers continued for much longer. The initial melt ejection velocities were up to 10 km/s, close to the velocity of the expanding gas, which entrained the melt particles, making their flight paths significantly longer than ballistic flight of small particles through a stationary atmosphere. The gas also buffered the entrained melt at high temperatures (~727-1727 °C), retarding cooling (especially by radiative heat loss from individual tektites), thereby allowing them sufficient time to form aerodynamic shapes and to lose volatiles (such as H_2O).

According to this model, different-sized particles from the Ries-type impact event experienced different thermal histories. At ~5 s after impact, the smallest tektite-type molten particles modeled (1.4 cm diameter) were at temperatures of approximately 3227 °C, while the larger particles (2.0 and 2.6 cm diameter) were at temperatures between 727 and 227 °C (Stöffler et al., 2002, their Fig. 8). At ~30 s after impact, the model indicates that all particles were buffered at approximately 727 °C. Although temperature predictions are only presented for 5-30 s after impact, final trajectories of the particles are shown and suggest that the largest (2.6 cm diameter) parcels traveled the farthest from the site of impact (~450 km), while the smallest (1.4 cm diameter) pieces landed less than 250 km away (Stöffler et al., 2002; their Fig. 9). All particles are modeled to have landed on the surface by 5-30 min after the initial impact (Stöffler et al., 2002).

While the simulation described in the previous two paragraphs provides a framework for thinking about the processes involved in tektite formation and some quantification of them, important questions remain unanswered. For example, although hydrocode models provide guidelines to direct our thinking about the temperature-time (*T*-*t*) history of an individual tektite

for a given impact event, such thermal histories will be controlled by many factors, including the angle of impact; the velocity, size, and composition of the impactor; the composition and porosity of the target material; the position and velocity of the tektite parent material (melt particles) in the ejecta plume; and the velocity and temperature of the ejecta plume (e.g., Artemieva, 2002; Artemieva et al., 2004; Johnson and Melosh, 2014). Moreover, these models do not currently provide detailed information about the later stages of tektite evolution, including how long tektites are entrained in and thermally buffered by the vapor, the *T-t* history of the vapor, or the time it takes to cool tektites to glass once they are no longer buffered by the vapor plume. These impact plume dynamics are among the least well understood aspects of impact processes, despite their influence on the effects that asteroid impacts have on local and global environments (Collins et al., 2012). Also, despite the long history of the study of tektites, there are very few quantitative constraints on their thermal histories (e.g., Arndt and Rombach, 1976; Wilding et al., 1996; Humayun and Koeberl, 2004) that can be used to test and constrain the output of the hydrocode models.

Geochemical investigations of tektites have shown that tektite glasses have high chemical resistance and slow devitrification kinetics (Heide et al., 2001; Osinski et al., 2012); contain mostly reduced iron ($Fe^{3+}/(Fe^{2+}+Fe^{3+})$ ~ 0.05; Giuli et al., 2010); and have low volatile contents: (<200 ppm H_2O, Koeberl, 1994); 50-160 ppm C and median values of 32 ppm F, 10 ppm Cl, and 3 ppm S, Moore et al., 1984). Other characteristics of most tektites are inclusions of lechatelierite (nearly pure SiO_2 glass; 99-100 wt. % SiO_2) and schlieren of glass with higher SiO_2 contents than the bulk tektite. Lechatelierite inclusions are generally thought to be the amorphous relicts of melted quartz grains (Fig. 1b) (e.g., Koeberl, 1986; Glass, 1990), although one study suggested that biogenic opal rather than quartz could be the precursor (Kinnunen, 1990). Lacroix (1915) proposed the name lechatelierite (in honor of Henry Le Chatelier) for the fused silica in fulgurite tubes formed by lightning strikes into sand.

The presence of lechatelierite in tektites was first described by Barnes (1940) in North American tektites. He wrote that it is "nothing more or less than fused silica (quartz)," and that

"fusion was rapid, that heat was intense, and that cooling was rapid" (Barnes, 1940; pp. 554). Although the size, abundance, and degree of vesicularity of lechatelierite have been used as qualitative indicators of thermal histories of tektites (Barnes, 1964), to our knowledge no modern studies have used lechatelierite inclusions in tektites to extract quantitative information about their *T-t* histories, except to assert that the presence of lechatelierite requires temperatures of at least 1700 °C (e.g., Barnes, 1958; Glass, 1990; Wilding et al., 1996; French, 1998; Howard, 2011; Schaller et al., 2016). Thermal histories of fulgurites, which also contain lechatelierite, have been estimated by Pasek et al. (2012), but direct comparisons cannot be made between fulgurites and tektites, as they are formed by different processes.

The study described in this paper was motivated by our expectation that there must be some diffusive relaxation of chemical gradients between lechatelierite and the surrounding felsic glass that formed during the early history of tektites when they were molten. As mentioned above, the tektites are usually inferred to have experienced temperatures of at least 1700 °C to account for the stable (as opposed to metastable) existence of molten SiO_2 (now quenched to lechatelierite), and perhaps even higher according to the hydrocode models described above. In this study, we first demonstrate that such gradients are ubiquitous and long enough that they can be well characterized and quantified. We then describe experiments that simulate the diffusion that produced these chemical gradients in natural tektites. Taken together, these descriptions of diffusive gradients between lechatelierite and felsic glass in tektites and the quantification of this diffusive process based on controlled laboratory experiments allow us to set limits on the thermal histories experienced by tektites during their formation and entrainment in the impact plume as they are ejected from the site of impact. The experiments also provide constraints on multicomponent diffusion in high-silica melts that will be of use in understanding magmatic processes on Earth and that extend our understanding of the phenomenology of diffusion in silicate melts.

3 METHODS

3.1 Description and analysis of natural tektite

The work presented here on natural tektites is restricted to a single sample, LTS1, which is a splash-form (tear-drop shaped) tektite ~6.5 cm long and 2 x 1.3 cm in cross section at its thickest point (Fig. 1a). The sample is from the private collection of Leon T. Silver and was originally collected in Thailand in a subfield of the Australasian strewn field (tektites collected in this area are known as indochinites.) Water content (total range from ~40-90 ppm) and major element chemistry (felsic/peraluminous) of the sample was reported in Newman et al. (1995). The tektite was sectioned into slabs (~750 – 850 μm thick) perpendicular to the long axis (Fig. 1). Sections were polished using alumina lapping films and 0.25 μm diamond paste for optical petrography, scanning electron microscopy, and electron probe microanalysis.

Backscattered electron (BSE) images were obtained using the Zeiss 1550VP field emission scanning electron microscope (FE-SEM) and JEOL JXA-8200 electron probe micro-analyzer (EPMA) with solid-state BSE detectors in the Division of Geological and Planetary Sciences Analytical Facility at the California Institute of Technology. Quantitative chemical microanalyses to determine major element concentrations along traverses across contacts between lechatelierite inclusions and the felsic host glass were collected using the JEOL JXA-8200 electron probe micro-analyzer (EPMA). Detection limits for each oxide were well below the measured abundances, ranging from a high of 0.06% for FeO to a low of 0.02% for K_2O, except for in the silica glass unaffected by interaction with the felsic glass. An accelerating voltage of 15 kV was used with a beam current of 10 nA defocused over a 5 or 10 μm spot (to minimize alkali loss) and counting times of 20 s on peak and 10 s each on high- and low-wavelength backgrounds. The spots were spaced ~5-10 μm apart so as to minimize overlap between analyses. Synthetic and natural mineral standards were VG-568 rhyolite glass (Si); synthetic TiO_2 (Ti); synthetic anorthite (Al, Ca); synthetic Cr_2O_3 (Cr); synthetic fayalite (Fe); synthetic Mn olivine (Mn); Amelia albite (Na); and Asbestos microcline (K). Data were reduced using a modified ZAF procedure (Armstrong, 1988). Average compositions of lechatelierite and

surrounding, far-field host tektite glass (averaged from data collected >200 μm from visible lechatelierite and schlieren) are given in Table 1.

3.2 Experimental methods

High-temperature melting experiments were conducted to generate textures and concentration profiles for comparison to those seen in natural tektites. Starting materials were mixtures of an indochinite tektite from the Caltech collection (CIT-17640b; similar in composition to LTS1 as determined by EPMA) and quartz from Hot Springs, AR (GRQ1). Compositions of tektite and quartz starting materials are given in Table 1. The indochinite was powdered in a tungsten carbide shatterbox and mixed by shaking with ~10 wt. % quartz grains (crushed in a Plattner's mortar and pestle and sieved to be 60-100 μm grains). The mixture was then pressed into ~300 mg pellets (with no binding agent) in a ½" diameter steel die (usually used to press KBr pellets for infrared spectroscopy).

Containerless melting experiments were carried out on chips from these pellets (~4-13 mg) using an aerodynamic levitation laser furnace (e.g., Pack et al., 2010) at the Institut de Physique du Globe de Paris (IPGP). The apparatus uses a 75 Watt CO_2 laser to heat samples while they are being levitated on a vertical stream of Ar gas flowing through a conical nozzle. This device allows short-duration, rapidly quenched, high-temperature experiments (maximum temperatures reached in this study were ~2400 ºC) to be performed without chemical interaction between sample and container walls. Sample temperature was controlled by adjusting laser power and was measured by optical pyrometry.

The experiments for this study required a multi-step heating process to achieve proper levitation: A 'fusion' step was first done at ~1300-1700 ºC for ~5-20 s to pre-melt the samples so they took on roughly spherical shapes suitable for levitation. The fusion step is not expected based on the diffusion coefficients reported below to result in significant diffusion between lechatelierite and surrounding glass during this step (diffusion distance would be <1 μm for a 5 s fusion at 1700 °C). The fusion step was followed by a quench to <900 ºC (lower limit of pyrometer), after which the temperature was increased to the final, target temperature of the

experiment (1800-2400 ºC). The sample was held at the final temperature for ~1-120 s. Table 2 lists run conditions for all experiments, and examples of *T-t* paths of some experiments are shown in Fig. S1. Experiments were quenched by turning off power to the laser while continuing levitation. The cooling rate upon quench from the high experimental temperatures (i.e., 1800–2400 °C) to the lower limit of the pyrometer (900 °C) is ~400-600 °Cs^{-1}. At this rate, it would take ~0.30-0.45 s to reach the glass transition temperature (T_g) of the felsic tektite matrix glass (~780 °C; Wilding et al., 1996), which would result in less than a 0.3 μm diffusion length scale based on our diffusion model presented in §4.2.3.

Run products from these experiments are dark-grey to black glassy spheres with diameters of ~1.5-2.3 mm and varying degrees of vesicularity. The spheres were cut in half at their widest dimensions using a wire saw, and one of the halves was mounted in epoxy and polished for imaging and analyses. BSE images were obtained for each charge using the ZEISS 1550 VP FE-SEM. The same instrument was used to conduct electron backscatter diffraction (EBSD) analyses to determine if quartz grains were melted, partially melted, or completely crystalline after heating. Unmelted grains and the crystalline portion of partially melted grains were determined to be α-quartz. Major-element concentration profiles across the boundary zone between silica glass, or lechatelierite (formed by quenching of liquid from melted quartz grains), and the felsic glass in experimental charges were measured using the JEOL JXA-8200 EPMA as described in §3.1.

4 RESULTS

4.1 Petrography of natural lechatelierite inclusions in tektites

4.1.1 Textures of lechatelierite inclusions in tektites

Figure 2 shows BSE images of lechatelierite inclusions in the natural indochinite tektite LTS1, representing a range of their sizes, shapes, and degrees of vesiculation. The lechatelierite grains are dark grey, whereas the enclosing felsic glass is a lighter grey due to the presence of elements heavier than Si. Inclusion sizes range from ~50 to ~500 μm in the longest dimension

visible in the plane of sectioning. Some inclusions are roughly equant (Fig. 2d-f) while others are elongated (Fig. 2c) or irregularly shaped (Fig. 2a). Vesicles are sometimes present in the felsic glass adjacent to lechatelierite (indicated by the 'A' labels in Fig. 2a, c, and d) or inside the lechatelierite inclusions (indicated by the 'B' labels in Fig. 2a-e). The vesicularity of the lechatelierite is generally higher than that of the felsic glass, ranging up to ~30% of the area of the inclusion.

Most lechatelierite inclusions are a uniform shade of dark grey, reflecting that they are uniformly ~100% SiO_2, but we observed two mottled or dotted with roughly circular lighter grey (i.e., lower SiO_2) regions (labeled 'C' in Fig. 2d and f). These light grey spots are similar in size to vesicles in other lechatelierite inclusions and likely formed by the filling of vesicles in the lechatelierite by felsic melt (see Table S1 for compositional data of these features). The boundaries between the lechatelierite inclusions and the felsic glass are generally rounded and convex outwards (e.g., label 'D' in Fig. 2d and e), but there are embayments, cusps, and irregularities (e.g., label 'E' in Fig. 2b-d) in these boundaries as well. These embayments into the lechatelierite of felsic glass are often associated with vesicles in the felsic glass, suggesting that the deformation of the boundary is due to the expansion of the vesicle at temperatures that were high enough to allow flow in both melts as the vesicle was growing (for more details on the origin of vesicles in tektites, see Barnes and Pitakpaivan (1962), Koeberl (1994), and references therein). A ubiquitous feature visible in the BSE images is a diffuse, intermediate grey halo (best seen at label 'F' in Fig. 2e) between the lechatelierite and host glass that is associated with concentration gradients in SiO_2 and other elements (described below) that formed by interdiffusion between the nearly pure SiO_2 melt and the enclosing felsic melt at the high temperatures at which tektites formed and evolved. Although these diffusion halos are present around every lechatelierite in the sample, they are not seen equally easily in all of the BSE images presented here due to differences in SEM conditions (e.g., brightness and contrast).

4.1.2 Compositional gradients between lechatelierite and adjacent felsic glass in natural tektites

Major element concentrations were obtained across the boundaries of lechatelierite inclusions in LTS1 along traverses starting in the felsic glass, crossing into the lechatelierite inclusion, and continuing out into the felsic glass on the opposite side of the inclusion, as indicated for example by the red line in Fig. 3a. Typical concentration profiles for the analyzed elements crossing lechatelierite-host glass contacts (Fig. 3b, c) confirm the indication from the intermediate grey halos around the lechatelierite inclusions (feature 'F' in Fig. 2) that there is a wide (>30 μm in the sample shown in Fig. 3a) boundary layer between lechatelierite and felsic glass defined by concentration gradients in oxide abundances. The silica content of the lechatelierite is essentially constant at ~100 wt% (grey shaded regions in Fig. 3b, c), but SiO_2 decreases abruptly in the surrounding felsic glass with increasing distance from the lechatelierite "boundary", defined by the break in slope in the concentrations of all elements at the location on the profile where the darker grey of the lechatelierite visibly begins to get lighter.

It is important to emphasize that although the "contact" between lechatelierite and felsic glass is unambiguous in the BSE images, in optical microscopy, and in the concentration profiles – reflecting the sharp increase in the gradient in SiO_2 at this point, this is not a boundary between two phases, but rather a continuous change in composition in a single material, i.e., glass; this gradient would be continuous if observed at a sufficiently fine scale, and even though lechatelierite is a named mineraloid and is often referred to as occurring as "grains", as if it were a distinct phase, there is no well-defined interface as there would be at a crystal-melt boundary. As emphasized below, the apparent abruptness of the "edge" of the lechatelierite reflects the strong concentration dependence of the diffusivity of SiO_2 and all the other elements as the SiO_2 content approaches 100%. Moving outward toward the felsic glass from the apparent "edge" of the lechatelierite, the gradient in silica content shallows progressively with distance (i.e., it is concave up in a plot of concentration vs. distance, although a point of inflection in the SiO_2 profile must occur somewhere near the apparent "edge" of the lechatelierite; see the forward

models of the evolution of the boundary zone developed below and shown in Figs. S2a and S2b as the SiO_2 concentration gradually reaches the background value (~72-75 wt%) of the far-field felsic glass.

As shown in Figs. 3b and 3c, the concentrations of all components other than SiO_2 decrease across the boundary layer from their far-field concentrations in the felsic glass to concentrations near zero immediately adjacent to the lechatelierite. All of these concentration profiles are asymmetric, becoming steepest towards the edge of the lechatelierite, and, with the exception of K_2O, all of the profiles are concave down across the entire boundary layer (although again there must be an inflection point in each profile near the lechatelierite that we have not observed directly due to the spacing of our data points but which can be seen in the forward models for Al_2O_3 shown in Figs. S2c and S2d. The K_2O profile is distinctive in that, relative to its far-field concentration, the concentration of K_2O first increases moving towards the lechatelierite, reaches a maximum, and then decreases with the characteristic concave downward shape close to the lechatelierite. Such a concentration profile is inconsistent with diffusion of K_2O down its own concentration gradient throughout the zone of interdiffusion between silica and felsic glasses.

The shapes of the concentration profiles are compared in Fig. 4, which shows the right side of Fig. 3b and 3c on a normalized scale (i.e., where 0 represents the minimum and 1 the maximum observed concentration for each element along the profile). On this normalized scale, the asymmetry of the profiles with respect to the Matano plane (defined by mass balance as intersecting the diffusion profile where the loss on one side is equal to the gain on the other side) and concave downward shapes of the gradients for all elements except SiO_2 are emphasized, as is the fact the systematic progression in the strength of the "bulge" toward the lechatelierite in the concave downward shapes from MgO and CaO, to Al_2O_3 and TiO_2, to Na_2O, to K_2O. These shapes are not consistent with a symmetric sigmoidal form passing through the midpoint of the original concentration step, such as one might predict for interdiffusion with constant (i.e., concentration-independent) diffusion coefficient, usually fit with an error function. Note that the observed shapes are consistent with strongly concentration-dependent diffusion coefficients (e.g.,

Crank, 1975; Delaney and Karsten, 1981; Behrens et al., 2007), as are to be expected in silicate liquids with variable SiO_2 content in which diffusion coefficients decrease towards pure silica liquid (e.g., Lesher and Walker, 1986; Koyaguchi, 1989; Baker, 1990; Behrens et al., 2004). Also notable in Fig. 4 is that despite the prominence of the "bulge" toward the lechatelierite in the non-SiO_2 oxide profiles, the lengths of all of the profiles are similar, which may at first appear to be surprising given that measurements of the diffusion coefficients of these oxides typically differ (e.g., Zhang et al., 2010 and references therein). Although only shown for a single boundary zone, Figs. 3 and 4 are representative of all such zones adjacent to lechatelierite that we have measured in indochinite LTS1 and in other tektites from both this and other strewn fields (Macris et al., 2017).

We note that plots of Al_2O_3, FeO, MgO, CaO, K_2O, and Na_2O vs. SiO_2 from the boundary layers adjacent to lechatelierite in the LTS1 indochinite (Fig. 5) are inconsistent with simple mixing, which would produce linear trends. Some oxides are concave up (e.g., MgO, FeO, and CaO) when plotted against SiO_2; Al_2O_3 is roughly linear; and others are concave down (Na_2O and K_2O). Consequently, although stretching, flow, and mechanical mixing could play some role in modifying these profiles, we will assume for the remainder of this paper that diffusion is the dominant process that generated the observed concentration gradients and boundary layers immediately adjacent to lechatelierite in tektites. In the following section, we describe experiments intended to test and quantify the hypothesis that the chemical gradients described above are generated by diffusion.

4.2 Experimental results

In this section, we describe the concentration profiles developed in the laser-heating experiments on mixtures of 10% crystalline quartz plus 90% bulk tektite and compare them to those described in the previous section at the boundary layer between lechatelierite and felsic glass in natural tektites. Such a comparison will allow us to test and quantify the hypothesis that

the chemical gradients observed in natural tektites are generated by diffusion and thus provide quantitative constraints on their thermal histories.

4.2.1 Textures of experimental run products

Figure 6 shows BSE images of cross sections of the run products from five levitation experiments done at 1800 °C, arranged in a sequence of increasing run duration from 1 s to 80 s. The sphericity of the run products reflects the low viscosity of the felsic melt (~90% of each sample) at the run conditions (~220 – 11 poise at 1800 – 2400 °C; Persikov, 1991). Although the 1800 °C experiments were all above the metastable melting temperature of quartz at 1 atm (1400-1450 °C; Mackenzie, 1960) and the liquidus of pure SiO_2 at 1 atm (1727 °C; Heaney, 1994), the quartz is incompletely melted in the shortest duration experiments. Crystalline quartz is readily distinguished from lechatelierite glass in BSE images by cracks and relief due to polishing contrast across crystalline quartz grain edges even though both phases are essentially pure SiO_2 (Fig. S3), and its presence in short-duration experiments was confirmed by EBSD; we did not detect any conversion of the quartz in the starting material to tridymite or cristobalite. Clear evidence of melting of the quartz grains is seen after 5 s at 1800 °C along the edges and in cracks of quartz grains closest to the edge of the sphere (Fig. S3b). The onset of melting always appears to begin on the outer edges of quartz grains and proceeds inward or in cracks. The 1800 °C experiment run for 80 s (Fig. 6e) shows evidence of complete melting of some quartz grains closest to the edge of the sphere (within the outermost 200 μm), but while some grains near the center of the sphere are also completely melted, some are only partially melted (Fig. S3e), suggesting the presence of temperature gradients. Concentration gradients are present at boundaries between lechatelierite and felsic glass in all experiments at 1800 °C, and these are visible in the BSE images as haloes (e.g., Fig. S3e). Comparisons of BSE images from experiments held for different times at 1800 °C (Fig. 6), show a decrease in number of vesicles in the felsic tektite glass with increasing time, with a simultaneous increase in vesicle size.

BSE images of the 2000 °C time series (Fig. 7 and Fig. S4) show textural trends with time that are similar to those observed in the 1800 °C experiments. Complete melting of some quartz

grains is observed along the outermost 200 μm of the sphere in the 5 s experiment, while some grains closer to the center show incomplete melting (Fig. S4a). The 10 s experiment also displays incomplete melting of some quartz clasts closest the center (Fig. S4b). The first observation of complete conversion of all quartz grains to lechatelierite is in the 2000 °C, 50 s experiment (Fig. 7c and Fig. S4c). Figure S4e shows in a BSE image an example of a diffusion halo surrounding lechatelierite. The longest experiment at 2000 °C was run for 120 s (Fig. 7e), and shows a significant decrease in the number of distinct lechatelierite "grains"; they appear to have been mostly eliminated by interdiffusion with the surrounding melt. As in the 1800 °C series, vesicles in the 2000 °C experiments become larger and less numerous with increasing duration, and they tend to concentrate toward the center of the sphere (Fig. 7). Another textural trend seen with increasing time at a single temperature is a progressive change from angular quartz grains to sub-angular lechatelierite to more rounded lechatelierite. A good example of this gradual softening or rounding of what started as sharp angles is seen in a visual comparison of the 2000 °C, 5 s experiment (Fig. 7a), with the 10 s experiment (Fig. 7b), and then the 50 s experiment (Fig. 7c).

In the 2200 °C series (Fig. 8 and Fig. S5), most of the quartz grains are melted by 5 s (Fig. 8a and Fig. S4a), except for a few near the center of the sphere. The 10 s experiment shows complete conversion of all quartz grains to lechatelierite (Fig. 8b). In the 50 s experiment, we see clear formation of schlieren (Fig. 8c), another texture common in tektites and observed in the indochinite LTS1 (Fig. 1b). The 80 s experiment also displays schlieren, although they are less distinct; and the lechatelierite is concentrated toward the center of the sphere (Fig. 8d). At 120 s, few schlieren or lechatelierite are still visible (Fig. 8e). Diffusion haloes are visible surrounding lechatelierite in some BSE images (e.g., Fig. S5b). Vesicles from the 2200 °C time series increase in size while decreasing in quantity from 5-50 s, and disappear completely by 80 s (although a cluster of vesicles could be missed due the plane of the polished section). During some experiments, bubbles were observed escaping at the surface of the levitating melt, evidence of the bubble-stripping scenario proposed by Melosh and Artemieva (2004) in which volatiles are stripped from low-viscosity tektite melts while at high temperatures by escaping bubbles.

Such motion of bubbles and the effects of sample rotation could be partly responsible for the production of schlieren.

Another notable point about the vesicles in these experiments is that no vesicles are observed inside of experimental lechatelierite (Figs. 6, 7 & 8). This is in contrast to the natural tektite where vesicles are found in both lechatelierite and felsic matrix glass (Figs. 1b & 2). According to Barnes and Pitakpaivan (1962), bubbles associated with lechatelierite in tektites are formed from "gas filled vacuoles" commonly found in quartz. However, we used high-purity, inclusion-free quartz from Hot Springs, AR to generate the experimental lechatelierite (Table 1), which may explain the lack of vesiculation compared with lechatelierite in the natural sample. While it is possible that other factors are contributing to the lack of vesiculation in the experimental lechatelierite (e.g., insufficient heating temperatures and/or times), more work would have to be done to investigate these variables independently.

One experiment was conducted at 2400 °C for ~1 s (Fig. S6). All quartz grains are completely melted and diffusion haloes are visible surrounding lechatelierite. Vesicles are present and are similar in size and quantity to the 2200 °C, 10 s experiment. Longer experiments at 2400 °C and higher temperatures were not explored because the sample started visibly evaporating (i.e., "smoking").

4.2.2 Compositional variations in experimental glasses

Electron microprobe profiles of major-element concentrations across 38 traverses across silica glass and felsic glass were obtained for all 20 of the experiments listed in Table 2. Concentrations of Al_2O_3, MgO, FeO, CaO, Na_2O, and K_2O are plotted vs. SiO_2 for traverses across the boundary layer between lechatelierite and surrounding glass (Fig. 9) for three experiments held for 80 s at 1800, 2000, and 2200 °C. Plots of oxides against SiO_2 for each traverse are concave up for some oxides (e.g., MgO, FeO, and CaO), roughly linear for Al_2O_3, and strongly concave down for others (Na_2O and K_2O). Loss of some oxides, including alkalis, SiO_2, and FeO, due to volatilization was observed in the felsic matrix glass (based on measurements taken at least 200 μm from lechatelierite inclusions or schlieren) in 2000 and 2200

°C experiments for longer duration runs (Fig. S7). This resulted in a concomitant increase in wt% for more refractory oxides, including Al_2O_3, MgO, and CaO, in the felsic glass matrices of the experimental glasses after heating in the levitation furnace (Fig. S7). These trends are generally consistent with the findings of Chapman and Scheiber's (1969) chemical trends for experimental fractional vaporization of tektite glass at 2000 °C in a vacuum furnace, reflecting changes in composition due to vaporization of more volatile elements at high temperature. As we did not measure the initial mass of our experiments (a precaution taken because of the delicate and friable texture of the starting material), we do not know the % mass loss of our experiments after heating, which prevents a rigorous comparison of the fractional vaporization results of the current study with those of Chapman and Scheiber (1969). Future experiments will investigate this aspect of tektite formation further; here we will focus on the lechatelierite-felsic glass boundary zones.

Oxide concentration profiles across the boundary zone between the lechatelierite and felsic host glass are similar for our experiments to those measured in natural tektite LTS1 in most respects: (1) the diffusion profiles are asymmetric for all oxides, becoming steeper as the lechatelierite is approached (Fig. 10); (2) the profiles mimic those of the natural sample and the experiments exhibit uphill diffusion of K_2O (Fig. 10c) similar to that seen in the natural tektite (Fig. 11); and (3) for the both the experimental and natural profiles, the length of the diffusion profiles across the boundary zone are basically the same for all oxides (Fig. 11). Indeed, visual comparisons of the shapes, lengths, and order of steepness of the concentration profiles across lechatelierite-felsic glass contacts from our experiments with those in natural tektite LTS1 reveal a near perfect match to an experiment heated to 2200 °C for 50 s (Fig. 11).

The lengths of the concentration profiles in the experiments increase with increasing time and temperature (Fig. 12 and Table 2), which is the behavior one would expect for a diffusively controlled process. The following section, §4.2.3, describes the systematic variation in profile lengths with increasing time and temperature in our experiments and how they can be used to estimate average diffusivities and extract activation energies at the temperatures investigated.

4.2.3 Interdiffusion profile length

The extent of the boundary layer, which we will refer to as the 'profile length,' is defined here as the distance between the points where a diffusion profile crosses 16 and 84% of its range (from highest to lowest concentration as determined by fitting a constrained spline curve to the data points along a traverse crossing from lechatelierite into surrounding felsic glass; e.g., see the blue shaded regions in Fig. 12). The profile lengths for non-alkali oxides from our experiments and natural tektite LTS1 are given in Table 2. In cases where a traverse was taken at a non-90° angle to the visible lechatelierite boundary, corrections were made to the profile's distance. However, we do not know the geometry of the inclusions with depth behind the polished surface of the samples seen in BSE images, or the angle of the 'cut' that is exposed at the surface. Inevitably, this will result in some unaccounted-for variability in the profile lengths reported here, but despite this potential issue, we observe systematic variations in the experiments: in particular, interdiffusion profile lengths increase with time at a constant temperature (Fig. 12) and with temperature in experiments held for the same amount of time. As a consequence of the increase in profile lengths with increasing time and temperature, the concentration profiles of most oxides become progressively less steep as temperature and time increase. This is not true, however, for K_2O, which instead becomes steeper close to the boundary with the lechatelierite because of increasingly exaggerated uphill diffusion behavior.

Plots of the SiO_2 profile lengths (experimental and natural) versus the profile lengths of the other non-alkali oxides fall on (or close to) a 1:1 line (Fig. S8), suggesting that silica diffusion from lechatelierite into the surrounding melt is the rate limiting factor controlling the counter-diffusion of the other components. Zhang et al. (2010) summarized that if strong major oxide concentration gradients exist in a diffusion couple, minor elements with intrinsic mobility (self-diffusivities) higher than that of SiO_2 often have concentration profiles with lengths similar to the SiO_2 profile lengths. This phenomenon has been explained as quasi-equilibrium "partitioning" between two liquids due to rapid diffusion (e.g., Watson, 1982; Richter, 1993; Zhang, 1993).

We can take advantage of the relationship between propagation of diffusion (distance) with time,

$$x \propto \sqrt{Dt} \quad (1)$$

where x is distance, D is diffusivity (which is assumed to be constant and can be approximated as a weighted average D when D depends on concentration), and t is time, to approximate diffusivities of major oxides in silica-rich melts from our experiments at 1800, 2000, 2200, and 2400 °C. Note that K_2O demonstrates uphill diffusion toward the more silica rich melt in both the natural sample and experiments (Fig. 11b), so this simple initial analysis cannot be applied to approximate the diffusivity of K_2O. Na_2O may be likewise complicated due to some combination of its extreme "bulge" toward the lechatelierite boundary (see Fig. 4) and loss by volatilization from the system, and is not quantified here.

Our definition of the profile length 16–84% rule described above has the advantage of using a large portion of the profile while avoiding the nearly flat parts where analytical error significantly influences the estimate of distance, hence minimizing relative error. The profile length defined this way can be shown to correspond to

$$x = \sqrt{7.91Dt} \quad (2)$$

in a simple diffusion couple with constant D, as described above for Eq. (1) (derivation in supplementary material). Hence, by plotting profile length versus the square root of time, we can estimate diffusivities for non-alkali oxides in our experiments. To illustrate this, plots of this type for SiO_2 and Al_2O_3 are shown in Fig. 13a and b, respectively. Plots for Fe, Mg, and Ca oxides are included in Fig. S9.

The slopes of the lines at each temperature in Fig. 13 and Fig. S9 are approximately equal to the square root of 7.91D at that temperature. The mean diffusivities of the non-alkali oxides obtained in this manner are shown in Fig. 14, plotted as ln$D$ (m^2/s) versus $10^4/T$ (K). The diffusivity of SiO_2 is known to vary significantly with its concentration (especially in silica-rich melts) and likewise to influence strongly the diffusivities of the other components in the melt (Zhang, 2010 and references therein). Thus, the diffusivities we obtain from our experiments

using Eq. (2) (Fig. 14) represent an average value for the ~75-100% SiO_2 compositional range across the profiles. (The dependence of D on SiO_2 concentration is discussed in more detail in §5.1.2.) Activation energies (E_a) can also be extracted from these data assuming the relationship

$$D = D_0 e^{-E_a/RT} \quad (3)$$

where D is diffusivity, D_0 is the pre-exponential factor, E_a is the activation energy, R is the gas constant, and T is the absolute temperature. Activation energies calculated from our experiments for Si, Al, Fe, Mg, and Ca oxides (Fig. 14, Table 3) are 399±11, 384±13, 391±13, 371±13, and 370±14 kJ/mol, respectively (errors are 2σ). Although SiO_2 is slightly higher based on errors, these are all similar, suggesting that a single activation process may be dominating the mobility of all these components. The D_0 values obtained using the profile lengths and Eq. (2) and (3) for these oxides are the same within error (Table 3). Taken together, the similarities in D_0 and E_a for all the oxides leads to the average D's spanning the boundary between lechatelierite and the felsic tektite glass for all the oxides being essentially indistinguishable over the temperature range of our experiments (Fig. 14f): As explained above, this result reflects directly the overall similarities in our experiments in the profile lengths of all of these oxides (Fig. S8), which in turn reflect the control exerted by SiO_2 concentration and diffusivity on the diffusion of the other oxides (Watson, 1982; Zhang, 1993).

5 DISCUSSION

5.1 Multicomponent diffusion in silica rich melts

The linear relationship between profile length and the square root of time for experiments at a single temperature (§4.2.3), plus the similarities between the concentration profiles across the lechatelierite-felsic glass boundaries in the experiments and in natural tektites, provides strong evidence that the dominant process recorded in these boundaries in tektites is diffusion at high temperature. In multicomponent diffusion (systems having three or more components), the diffusion of a given component depends not only on its own concentration gradient but also on those of all of the other components in the system (e.g., Zhang, 2010). The asymmetric shapes of

the profiles in our experiments and the anomalous behavior of K_2O demonstrate that the complex effects of multicomponent diffusion had considerable influence on the development of the diffusive profiles in the silica-rich melts in the boundaries between lechatelierite inclusions and the dominant felsic glasses in tektites.

5.1.1 Uphill diffusion

Diffusion of a component up its own concentration gradient, so-called 'uphill' diffusion, has been observed before in natural silicate systems and reproduced in experiments involving diffusion between melts of contrasting SiO_2 content. Sato (1975) first reported an apparent enrichment of alkalis (particularly K) in diffusion coronas around quartz xenocrysts entrained in Neogene andesite and basalt lavas from Shikoku, Japan. The anomalous enrichment was reproduced in experiments at 1400 °C on a mixture of finely ground basalt and quartz crystals, confirming that alkalis diffused against their concentration gradients toward the more highly polymerized silica-rich composition. To explain these observations, Sato (1975) presented a model in which the uphill diffusion behavior reflects the non-ideality of alkalis in Si-rich melts (i.e., the activity coefficients of $KAlO_2$ and $NaAlO_2$ increase as SiO_2 concentration decreases). Sato (1975) concluded that diffusion is driven by and proceeds down the chemical potential gradient of a component, even when that component exhibits apparent uphill diffusion against its concentration gradient.

Subsequent experimental studies confirmed and elaborated on the work of Sato (1975) regarding uphill diffusion of alkalis in silicate melts. Watson (1982), Fisk (1986), and Koyaguchi (1989) observed uphill diffusion of alkalis in experiments investigating interdiffusion of molten basalt with granite, harzburgite, and dacite, respectively. Experiments on diffusion-limited dissolution of quartz into andesitic melt by Zhang et al. (1989) resulted in strong uphill diffusion of K_2O. However, Baker (1990) did not see evidence of uphill diffusion in diffusion couple experiments between molten rhyolite and dacite. In all studies discussed here where uphill diffusion was observed, the alkalis diffused uphill toward the more silicic melt. This is also true of our experiments and can be explained by the inverse relationship between the activity

coefficients of alkalis and silica content in silica-rich melts (Sato, 1975; Watson, 1982): That is, the activity coefficients of the alkali oxides decrease with increasing silica content, such that to have the same chemical potential of K_2O in a more silicic melt relative to a less silicic melt, the concentration of K_2O must increase, resulting in the "uphill" behavior of the concentration profiles approaching more Si-rich compositions along the lechatelierite-felsic glass boundary layer; the maximum in K_2O within the diffusive boundary layer in our experiments and in the natural tektite reflects the competition between this effect of silica content on the activity coefficient of K_2O and the fact that the K_2O concentration must approach zero as the pure silica melt is approached, such that K_2O — and the resulting decrease in the activity of K_2O due to the decrease in its concentration — eventually overwhelms the effect of silica content on the activity coefficient of K_2O.

The SiO_2 profiles in the present study can be treated by the effective binary diffusion approach developed by Cooper (1968). With this approach, we simplify the treatment of multicomponent diffusion, which depends on many unknown parameters in this system, by assuming that it behaves effectively as a binary diffusion couple, with SiO_2 being one component and all the other oxides being combined into the counter-diffusing component. Other monotonic concentration profiles can be treated similarly. Note, however, that uphill diffusion profiles cannot be reproduced in this way and must either be treated by empirical models (e.g., Zhang, 1993), multicomponent and composition-dependent diffusion matrices (e.g., Trial and Spera, 1994; Guo and Zhang, 2016; Guo and Zhang, 2018), or models that couple the compositional dependence of the chemical potentials of components in silicate melts with diffusion (Richter, 1993). Development of such models is beyond the scope of this work, so we do not attempt quantification of the uphill diffusion observed for K_2O.

5.1.2 Evidence and treatment of multicomponent diffusion in tektites and experiments

In this section we model the concentration profile of SiO_2 in the diffusive boundary zone between the lechatelierite and felsic glass by assuming (1) that the diffusivity of SiO_2 depends exponentially on its own concentration in the melt (and not on the concentrations of other oxides

individually), and (2) that its coupling to other components in our experiments can be approximated with the effective binary diffusion (EBD) approach developed by Cooper (1968) and used by Zhang et al. (1989) in their study of SiO_2 diffusion during quartz dissolution into rhyolitic melt. With these assumptions, we simplify the treatment of diffusion, which depends on many unknown diffusive and thermodynamic parameters in the compositionally complex tektite plus quartz system by assuming that it behaves effectively as a binary diffusion couple, with SiO_2 being one component and all the other oxides being combined into a single counter-diffusing component.

The SiO_2 concentration profiles from our experiments have an asymmetric shape (i.e., the steepest portion is closest to the lechatelierite) that indicates a low diffusivity as the SiO_2 content of the melt approaches 100 wt% and higher diffusivity at lower SiO_2 concentrations; a simple (though likely incomplete) explanation of this phenomenon is that the diffusivities of most components decrease with increasing SiO_2 content because the polymerization of the melt increases with increasing SiO_2 content. The relationship between ln*D* and SiO_2 concentration is often observed to be approximately linear (e.g., Lesher and Walker, 1986; Koyaguchi, 1989; Behrens et al., 2004; Ni et al., 2009). Assuming this to extend to the high silica contents of melts in the lechatelierite–felsic melt boundary zone, we approximated the SiO_2 diffusivity with the following functional form:

$$D = D_1 e^{aC} \quad (4)$$

where *D* is the effective binary diffusion coefficient of SiO_2 at a given SiO_2 concentration (m^2/s); D_1 is SiO_2 diffusivity approaching 100 wt% SiO_2, assumed to be dependent on temperature via an Arrhenius relationship, $D_1 = D_1^0 e^{-Ea/T}$, where D^0_1 is the diffusivity approaching 100 wt% SiO_2 at infinite *T* (K) and E_a is its activation energy, which is assumed to be independent of composition; *a* is a constant, independent of composition and temperature; and *C* = (100 - SiO_2*) (wt%). The EMPA analyses of SiO_2 concentration at spots on the lechatelierite is sometimes greater than 100 wt%, and this results in some numerical difficulties in modeling. To avoid this difficulty, we applied a correction to anomalously high SiO_2 values by defining SiO_2* = SiO_2 +

100 – oxide total, for all points along the profile.

Given equation (4), the diffusion problem near the lechatelierite-felsic melt boundary can be treated as a diffusion couple with concentration-dependent diffusivity as given in Eq. (4). Because the length of the diffusion profile (e.g., ~5–30 μm, Fig. 12) is typically much smaller than the diameter of the lechatelierite (~100 μm, Fig. 2), we assumed a one-dimensional diffusion geometry. The diffusion problem is solved numerically using the explicit finite difference method. Figure 15 shows an example of this model applied to an experiment run at 2000 °C for 5 s. The fit has an $r^2 = 0.99982$. Fits were done for profiles from between one and four experiments at each temperature, in which the geometry of the lechatelierite allowed for the one-dimensional diffusion couple, and having enough data points along the traverse for robust fitting. The initial fits allowed both a and D_1 as fitting parameters, but the variation of the a parameter from one experiment to another is uncorrelated with temperature and has large errors. Based on the results of these initial fits, the parameter a was fixed at a value of 0.12, and only D_1 was allowed to vary to fit a given concentration profile. If there were two or more profiles fit at a single temperature, then D_1 was still allowed to vary in each profile (rather than using one single D_1 value to fit all profiles at this temperature), meaning that there could be different D_1 values at a single temperature. Although a may depend on temperature, our data are not sufficient (e.g., only 5 or 6 points in Fig. 15 have concentrations intermediate between pure SiO_2 and the felsic glass) to resolve the dependence clearly. Figure 16 shows the fit values of D_1 (SiO_2 diffusivity approaching 100 wt.% SiO_2; blue diamonds), the value of D at 75% silica (green diamonds), and their temperature dependence (and the corresponding composition independent fit to E_a; blue and green lines). Also shown for comparison is the "average" D value for each experiment based on fitting our experimental data to Eq. (2) (individual fits are shown as pink diamonds and the best fit line is in pink).

As mentioned above in connection with motivation for Eq. (4), an exponential dependence of the diffusivity of SiO_2 on composition has been demonstrated before. Lesher and Walker (1986) and Koyaguchi (1989) determined the diffusivity of SiO_2 between basaltic and

more felsic melts at 1300-1500 °C at 10 kbar with SiO_2 concentrations ranging from 50-75 wt%. Koyaguchi (1989) report 0.8 wt% H_2O in their experiments; although Lesher and Walker do not report H_2O concentrations there is likely some H_2O present since even nominally anhydrous piston-cylinder experiments contain small amounts of H_2O (e.g., Laporte et al., 2004; Hauri et al., 2006; Médard et al., 2008). The results from these two studies, shown in Fig. 17 as $\ln D_{SiO_2}$ vs. wt% SiO_2, illustrate that the diffusivity of SiO_2 decreases exponentially as SiO_2 concentration increases (as indicated by the linear relationships on the semi-logarithmic plot) and support the use of this functional form in fitting our experimental data using Eq. (4). Also, the slopes of their $\ln D_{SiO_2}$ vs. wt% SiO_2 functions are similar to the best fit a value based on our fit to the SiO_2 concentration profiles in our experiments. Note that Baker (1990) also investigated SiO_2 diffusivity between dacite and rhyolite melts in anhydrous, 1 atm experiments at 1200-1393 °C, but his results do not support the same simple decrease in $\ln D_{SiO_2}$ with increasing silica content: these results, also shown in Fig. 17, show a weaker dependence of the logarithm of SiO_2 diffusivity with increasing concentration, except for the 1393 °C experiments, which have an anomalous positive slope; such a relationship between $\ln D_{SiO_2}$ and silica content would not be compatible with the concentration profiles we have observed in our experiments or the natural tektite. Yu et al. (2015) examined SiO_2 diffusion during quartz dissolution in rhyolitic and basaltic melts; although they observed a negatively sloped linear relationship (not shown in Figs. 16 and 17) between $\ln D_{SiO_2}$ and SiO_2 concentration (Eq. (4)) within each experiment, but obtained a better overall linear fit to combined data spanning basaltic to rhyolitic compositions by plotting $\ln D_{SiO_2}$ versus the sum of Si+Al cation mole fractions. We have not explored this alternative compositional dependence because the simpler dependence on silica content alone leads to excellent fits to our measured profiles.

Comparison of the results obtained from fitting our experimental profiles (using Eq. (4)) with these previous experimental studies are presented in Fig. 17. Colored lines represent the fits to data from this study, which span the composition space from 75 to 100 wt% SiO_2, and are fit by taking the log of Eq. (4) to obtain the following an equation for the dependence of SiO_2

diffusivity on composition and temperature at 1 atm:

$$\ln D_{SiO_2} = -0.12W - \frac{48605\ (\pm 5019)}{T} + 3.23\ (\pm 2.14) \quad (5)$$

where D is diffusivity in m^2/s, W is the concentration of SiO_2 (wt%) and T is temperature (K). Our results at 2000 °C, 1 atm overlap those of Lesher and Walker (1986) at 1475 °C, 10 kbar (Fig. 17), which at first glance might seem problematic, but is not necessarily unreasonable considering the differences in pressure, overall melt composition, likely water content, and experimental set-up (diffusion couple vs. Soret diffusion experiments) from the two studies. The diffusivity of components (major and minor) in a silicic melt are known to increase dramatically with increasing water content (e.g., Mungall and Dingwell, 1997; Behrens et al., 2007), and also significantly with increasing pressure (e.g., Baker, 1990). Direct comparison of the 1 atm experiments of Baker (1990) with those of this study reveal generally consistent trends in D_{SiO_2} with temperature and composition (Fig. 17). However, our experiments do not match up with those of different compositions at lower temperatures, and should not be extrapolated to lower SiO_2.

Figure 16 shows a summary of SiO_2 diffusivities vs. $10^4/T$ from this study: Each blue diamond is based on the best fit to the SiO_2 concentration profile in an experiment using Eq. (4), followed by a calculation from that fit using Eq. (4) of D_{SiO_2} at 100% SiO_2; each green data point shows the calculated values of D_{SiO2} at 75% SiO_2 based on the fit to Eq. (4). The blue and green lines are linear regressions through the same color diamonds, the equations of which are used to determine D_0 and E_a values (Table 3). The pink data points (and best fit line) are the D_{SiO_2} values derived from interdiffusion profile lengths using Eq. (2) (these are reproduced from Fig. 14a); as emphasized above, these are not associated with a well-defined SiO_2 content, but represent an average value for the profile spanning 75-100% SiO_2 and thus the fact that these estimates of

D_{SiO_2} plot between those for 100 (blue) and 75% (green) SiO_2 based on fitting the details of the full profiles to a concentration dependent D_{SiO_2} function is confirmation of the internal consistency of our two approaches to extracting D_{SiO_2} values from our experimental data. Activation energies associated with fits to D_{SiO_2} based on either equation (2) or (4) are also listed on Fig. 16 (and in Table 3), and they are the same within error (reported as 2σ) for either treatment of the data.

Figure 16 also shows summaries of D_{SiO_2} values and activation energies from previous experimental studies. The dashed line represents the estimated temperature dependence of SiO_2 diffusivities at 55 wt% SiO_2 reported in Koyaguchi (1989), obtained by combining the results of their experiments with those of Watson (1982) according the equation given by Koyaguchi (1989): $\log D\ (cm^2/s) = 3.6 - 18{,}000/T\ (K)$, which results in an activation energy of ~345 kJ/mol. SiO_2 diffusivities calculated by us from experiments by Baker (1990) at 65, 70, and 75 wt% SiO_2 are plotted as open triangles, circles, and squares, respectively. These data are combined to give an activation energy of 440±15 kJ/mol. Given the differences in experimental techniques, temperature and pressure, melt composition, and data analysis, we find the general agreement in the derived activation energies for silica diffusion to be surprisingly good.

The concentration profiles of all non-alkali oxides other than silica are overall similar in shape (Fig. 4) and different from those of silica. Using Al_2O_3 as a representative of these other oxides, we used Eq. (4) to model the shapes of its concentration profiles much as we did for SiO_2. Al_2O_3 diffusivities were determined from our experimental profiles using Eq. (4), where C = wt% Al_2O_3 and a = 0.23 (See Fig. 15c for an example fit). As for this same approach applied to fitting the silica profiles, the fits to this simple parameterization of the compositional and temperature dependence capture well the details of the concentration profiles, including the downward curvature as the lechatelierite is approached; the apparent break in slope in the alumina profile at the "edge" of the lechatelierite (which is actually continuous but appears discontinuous due to a strong upward curvature of the profile as $D_{Al_2O_3}$ and $C_{Al_2O_3}$ both approach zero), and the retrenchment and softening of the "edge" of the lechatelierite with time. Fig. S10

shows $\ln D_{Al_2O_3}$ vs. $10^4/T$ at ~0% Al_2O_3 (i.e., the edge of the lechatelierite) and at 13% Al_2O_3 (i.e., in the felsic melt); each data point represents a calculation using Eq. (4) based on the parameters resulting from the fit to the Al_2O_3 concentration profile. Also shown are $\ln D_{SiO_2}$ vs. $10^4/T$ for the fits described above for the silica profiles to Eq. (4), at ~100% and 75% SiO_2 (also shown in Fig. 16).

We also found that using the profile length approach to determine the diffusivities and activation energy of Al_2O_3 (i.e., based on Eq. (2); see Fig. 14) gives roughly the same result as those of SiO_2, although the profiles are strikingly different. These results agree with the diffusivities presented in §4.2.3 using the interdiffusion profile lengths and Eq. (2), and further emphasize the result that SiO_2 is controlling the diffusivity of other components in the melt. Figure S10 also shows how the diffusivities of Al_2O_3 also depend on composition along the profiles and mimic the variation in D_{SiO_2}; i.e., the diffusivities are lowest at points closest to the lechatelierite corresponding to ~100 wt% SiO_2 and ~0 wt% Al_2O_3, and highest in the far-field felsic glass were SiO_2 decreases to ~75 wt% and Al_2O_3 to ~13 wt%. Figure S2 shows the predicted time evolution of the SiO_2 and Al_2O_3 profiles based on this treatment, and Fig. S11 illustrates the retrenchment of the "edge" of the lechatelierite (defined as the point of maximum curvature on the profile) with time. These figures emphasize the increase in profile width with time, the preservation of the strong asymmetry in the profiles with time, and the retrenchment of the lechatelierite inclusions with time (i.e., its "edge" moves inward as the profile evolves).

In closing this section, we want to emphasize its importance. The complexity of the concentration profiles between the lechatelierite and felsic glass in the natural tektites and in our experimental run products might at first seem to preclude simple quantitative analysis and modeling of their details. Indeed, the uphill diffusion of K_2O and understanding the progressive shift in the magnitude of the "bulge" toward the silica-rich edges of the profiles of oxides other than SiO_2 (i.e., from MgO and CaO, which have the smallest bulge to Na_2O and K_2O which have the largest) will surely require a treatment that couples the complex thermodynamics of these silica-rich melts with diffusion. However, this section demonstrates that the overall evolution of

the boundary zone length with time and temperature *and* the details of the concentration profiles of the two most abundant oxides in the system, SiO_2 and Al_2O_3, can be reproduced in detail with relatively simple treatments of the strong concentration dependence of D_{SiO_2} and $D_{Al_2O_3}$, and in the case of SiO_2, one that incorporates a long-known exponential dependence of silica diffusivity on silica concentration. This not only permits understanding to how some of the curious features of the observed concentration profiles form (e.g., the very sharp boundary between the lechatelierite and the adjacent boundary zone which, though continuous, looks very much like the edge of a dissolving crystalline phase) but also will enable detailed modeling of concentration profiles that would form during arbitrary and potentially complex thermal histories, which could be key to interpreting the details of the concentration profiles observed in natural tektites.

5.2 Implications for thermal histories of tektites

The average interdiffusion profile lengths of SiO_2 and Al_2O_3 from seven lechatelierite boundaries in the natural tektite, LTS1, are ~19 μm (shown as a dashed grey line in Fig. 13; data used for determining the average in Table 2). By finding the intersection of the natural tektite's average profile length with the trends generated by fitting a linear regression to the experimental profile lengths with the square root of time (Figs. 13 and S9), we can estimate the times required at any temperature to produce these profiles by isothermal heating of the natural sample. For example, by dividing the natural profile length (~19 μm for SiO_2) by the slope of the line fit through the 2200 °C data in Fig. 13 (3.83 $\mu m/s^{1/2}$), we get ~5 $s^{1/2}$, or ~25 s. Although Fig. 13 only shows the results for SiO_2 and Al_2O_3, similar estimates for permissible isothermal *T-t* histories consistent with the length of the profiles in the natural sample (Table 2) were obtained for each of the non-alkali oxides measured (Fig. S9), and all of these data were used to calculate independent isothermal heating *T-t* estimates in this manner.

Figure 18 shows the family of possible isothermal solutions consistent with the average profile length from natural tektite, LTS1, based on the profile lengths and experimental results for each oxide. According to these solutions, this Australasian tektite could have been entrained

in an impact vapor plume at 2400, 2200, 2000, and 1800 °C for ~3, 25-33, 59-74, or 521-699 s, respectively. As we are modeling an isothermal process, we envision extremely fast initial heating (from the initial energy of the impact), followed by buffering at high *T* by an enveloping, hot impact vapor plume for some period of time, followed by extremely fast quenching to below the glass transition temperature upon the melt escaping the plume or plume dissipation, as how this condition may be achieved. Our isothermal model assumes negligible interdiffusion of components during the quick heating and quenching (an alternative model is presented later in the section). Although there is a bigger range in the required duration at the lower-temperature, longer-time fits, given the fact that the profile lengths (Fig. S8) and the ln*D* vs. $10^4/T$ (Fig. 14f) plots are similar, it is inevitable that all of the oxides give similar results. Because the activation energies of all the oxides are essentially identical, we cannot deduce a unique isothermal *T*-*t* constraint here, but instead can only present these estimates as a family of possible solutions (Fig. 18). Another element or isotope with a different activation energy that is not controlled by SiO_2 content along the profile would provide the information required to estimate a unique isothermal history (i.e., both *t* and *T*) that could produce the observed profile lengths.

Figure 19 shows the result of running a forward model using the relationship described in Eq. (4) and the corresponding SiO_2 diffusivities at 2000 and 2200 °C for varying times (colored lines) from 0-120 s. The open circles superimposed on these curves in Fig. 19 are data from the natural tektite (LTS1), indicating that the temperature of the natural sample could have been (based only on SiO_2 and neglecting the fits of other components) buffered by a 2000 °C impact plume for 50-120 s, or a 2200 °C plume for 25-50 s. These conditions are consistent with those indicated by the profile length treatment: 2000 °C for 53-77 s and 2200 °C for 28-34 s (Fig. 18). The fact that the forward model predictions of time scales required to produce the natural profiles are similar whether the shape of the full concentration profile is used (as we have described here using Fig. 19) or whether only the overall profile width is used (as described in the previous paragraph) reflects the agreement in the inferred D_{SiO_2} whether averaged over the profile length (i.e., using Eq. (2)) or obtained from fits to the full concentration profile assuming

a concentration dependent diffusivity (i.e., using Eq. (4)) (see Fig. 16). As emphasized earlier, this consistency from these different approaches to converting the results of our experiments into quantitative estimates of diffusivities and their temperature dependence provides flexibility and confidence to quantitative applications of the results of our experiments to natural samples. In addition, direct comparison of the topologies of all oxide concentration profiles across lechatelierite-matrix glass contacts from our experiments reveals that the experiment that most closely matches the natural sample in terms of shape and length of all oxides (including the distinct shape of the uphill diffusion of K_2O of the natural tektite) was held at 2200 °C for 50 s (Fig. 11), which is also in agreement with estimates based on (Figs. 18 and 19).

Although diffusion at constant temperature is plausible for natural tektites (e.g., if they were thermally buffered by the impact plume), our data can also be used to constrain alternative thermal histories (e.g., Stöffler et al., 2002). Diffusion during more complex thermal histories can be treated rigorously, provided that the times quoted above are interpreted to be the effective diffusion time scale in the melt state, $\tau = \int Dot/D_{T_0}$ where D_{T_0} is diffusivity at the initial temperature T_0 (e.g., Zhang, 2008, eq. 3-56a). For example, if only considering the profiles to be due to diffusion during cooling (i.e., after the tektite material was heated up, melted and ejected, and no longer buffered by a hot impact vapor plume), we use asymptotic cooling (Zhang, 2008) to approximate the cooling in a tektite:

$$T = T_0/(1 + t/\tau_c) \quad (6)$$

where the cooling time scale $\tau_c = T_0/q_0$; T_0 is the initial peak temperature; and q_0 is the initial cooling rate. In this case, the effective diffusion time scale can be calculated from

$$\tau = \tau_c/[E_a/(RT_0)] \quad (7)$$

where E_a is the diffusion activation energy and R is the gas constant (e.g., Zhang, 2008, eq. 3-56c). For E_a = 392 kJ/mol and the effective diffusion time scales derived above for 2400, 2200, 2000, and 1800 °C, respectively, the cooling time scales would be 53, 477, 1369, or 15373 s. The conductive-convective cooling time scale for a cm-sized clast like LTS1 is of the order 90 s, based on comparison to the cooling rate of obsidian clasts cooled in compressed air streams (Xu

and Zhang, 2002). Thus, in the context of this asymptotic model cooling history (assuming no diffusion during heating up and a dwell time of zero at the peak temperature), the observed diffusion profiles in LTS1 coupled with the estimated cooling time scale suggest a peak temperature of 2357 °C, a cooling time scale of 90 s, and an effective diffusive time scale of 5 s. This cooling time scale is consistent with the cooling rate obtained by Wilding et al. (1996) of 1 to 10 K/s (cooling rate at the glass transition temperature, ~780 °C). For example, using T_0 = 2357 °C, and a cooling time scale of 90 s, the cooling rate at 780 °C is 4.7 °C/s, which is consistent with the range given by Wilding et al. (1996), whereas cooling rates assuming an asymptotic model cooling history with T_0 =2000 °C/s (0.36 °C/s) or 1800 °C (0.035 °C/s) are outside the range given by Wilding et al.

Peak temperatures of 2000-2400 °C are on the same order of, but higher than those predicted by hydrocode models of tektite-producing impacts by Artemieva et al. (2004) and Stöffler et al. (2002). Artemieva et al. (2004) calculate peak temperatures between 727 and 1727 °C for an expanding vapor cloud in contact with tektite parent material produced by the 20 km/s impact of a 1 km projectile at a 30° angle; although there are substantial uncertainties in the equations of state used in the models and no time estimate is provided (that we could find) associated with these temperatures to indicate how long the melt was entrained in the hot vapor plume, we can confidently rule out peak temperatures much below 1800 °C unless quartz melts metastably (i.e., given the fact that lechatelierite is ubiquitous in tektites). Moreover, based on the asymptotic cooling constraints of the previous paragraph, the cooling time scales required to produce the observed diffusion profiles between silica melt and felsic melt would have to have been several hours (~4) for a peak temperature of 1800°C, to several days (~10) for 1500 °C, to many years (~1431) for 1000 °C, and these are likely prohibitive for any plausible cooling environment for tektites (e.g., Stöffler et al., (2002) report that particles typically land on the surface between ~5-30 minutes after impact). Stöffler et al. (2002) predict that the expanding gas, which entrains the melt particles, will buffer their temperatures at between 727 and 1727 °C as well. However, their model predicted that different sized particles experience different thermal histories (Stöffler et

al., 2002, their Fig. 8). The smallest particles modeled are 1.4 cm in diameter and are initially at temperatures of approximately 3227 °C, while the largest particles are 2.6 cm in diameter and start at temperatures between 227 and 727 °C (Stöffler et al., 2002; their Fig. 8). At 30 s, all particles are buffered at approximately 727 °C, but there is no information reported as to how the temperature will change after that. We emphasize that estimates for the thermal history of an Australasian tektite based on our experiments should not be directly compared with the hydrocode models of Artemieva et al. (2004) or Stöffler et al. (2002) because the impacts these studies attempt to reproduce are likely smaller than the impact that produced the Australasian strewn field.

The constraints on thermal history provided by our experiments and applications to natural tektites can be used to inform future models of impact ejecta processes, and in particular, such models should strive for consistency with the *T-t* constraints provided by our data. Furthermore, the diffusion behavior of SiO_2 between lechatelierite and tektite matrix glass can be applied to tektites from other strewn fields and from different distances and ejection azimuths within a single strewn field in order to gain a better understanding of impact plume dynamics. Future applications of this new tool for studying impact ejecta may lead to empirically based thermal maps of past impacts.

6 CONCLUSIONS

1. Concentration profiles ~20 μm in length were discovered in an Australasian tektite at the boundaries between lechatelierite inclusions and the felsic glass that encloses them. The profiles formed by multicomponent diffusion between silica melt (quenched to 'lechatelierite') and felsic melt, after melting due to the hypervelocity impact that produced the tektite, but before quenching to glass. These profiles are readily measurable and can be used to constrain the *T-t* paths of tektites and the models of the thermal evolution of ejecta of the impacts that produced them.

2. All major aspects of the diffusion profiles between lechatelierite and surrounding felsic glass were successfully reproduced via experiments on mixtures of powdered natural tektite plus ~10 wt% quartz grains (60-100 μm) that were exposed to temperatures of 1800-2400 ˚C for 1–120 s in an aerodynamic levitation laser furnace, including: diffusion length scale, the strong asymmetry of the concentration profiles, the similarities in lengths of the diffusive profiles for all non-alkali oxides, and differences in the shapes of the concentrations profiles among the oxides.
3. The characteristic lengths of concentration profiles across experimentally produced lechatelierite-felsic glass boundaries for all non-alkali oxides are proportional to the square root of the experiment duration, allowing the derivation of diffusivities and activation energies; the results of which are consistent with measurements in melts with lower SiO_2 contents and at lower temperatures reported in the literature.
4. The full experimental concentration profiles of SiO_2 and Al_2O_3 were also fit using simple formulations of the dependence of their diffusivities on SiO_2 content and temperature; the derived diffusivities and their temperature dependences are similar to those obtained from the $\sqrt{t}$ dependence of the characteristic profile lengths.
5. The two diffusion treatments presented in this work allow for estimates of the thermal history of the natural tektite in which the boundary layers were discovered: (i) assuming that the interdiffusion between the silica and felsic melts occurred at a constant temperature, examples of possible solutions include heating at ~2000 °C for ~70 s, ~2400 °C for ~3 seconds; (ii) alternatively, assuming that the diffusion profiles were the result of a non-isothermal event, examples of possible asymptotic cooling histories include a characteristic cooling time scale of ~50 s for a maximum temperature of 2400 °C, and cooling time scale of ~1400 s for a maximum temperature 2000 °C. Further, a maximum temperature of ~2360 °C would yield an effective diffusive time scale of ~5 s with a cooling time scale of ~90 s, which gives a cooling rate at the glass transition temperature of ~5 °C/s; results that are consistent with independent estimates of cooling time scales

for ~1 cm rhyolitic clasts in air (Xu and Zhang, 2002), as well as previously determined tektite cooling rates at the glass transition temperature (Wilding et al., 1996). Although this relatively simple cooling model thus satisfies our measurements of boundary zone thickness between lechatelierite and felsic tektite glass, our experimental constraints, and the constraints on cooling rate from Xu and Zhang and Wilding et al., more complex *T-t* paths are possible; the thickness of the boundary zone surrounding lechatelierite implied by any such model can be modeled using our experimental results and compared to measured thicknesses in tektites.

7 ACKNOWLEDGEMENTS

The authors would like to acknowledge NASA grants NNX12AH63G and NNX15AH37G for funding this study. We also thank Peter Goldreich and Megan Newcombe for insightful discussions and modeling advice. Thanks to John Shuckle for his coding expertise. Chi Ma's help was invaluable in obtaining the electron probe data. This manuscript was greatly improved by the comments of Mathias Ebert and two anonymous reviewers.

8 REFERENCES

Ahrens T. J. and O'Keefe J. D. (1972) Shock melting and vaporization of lunar rocks and minerals. *The Moon* **4**, 214–249.

Armstrong, J. (1988) Quantitative analysis of silicate and oxide minerals: comparison of Monte Carlo, ZAF and phi-rho-z procedures. *Microb. Anal.* **23**, 239-246.

Arndt J. and Rombach N. (1976) Derivation of the thermal history of tektites and lunar glasses from their thermal expansion characteristics. Proceedings of the 7th Lunar and Planetary Science Conference. pp. 1123–1141.

Artemieva N. (2002) Tektite Origin in Oblique Impacts: Numerical Modeling of the Initial Stage. In *Impacts in Precambrian Shields* (eds. J. Plado and L. J. Pesonan). Impact Studies. Springer, Berlin, Heidelberg. pp. 257–276.

Artemieva N., Karp T. and Milkereit B. (2004) Investigating the Lake Bosumtwi impact structure: Insight from numerical modeling. *Geochem. Geophys. Geosyst.* **5**, 1-20.

Baker D. R. (1990) Chemical interdiffusion of dacite and rhyolite: anhydrous measurements at 1 atm and 10 kbar, application of transition state theory, and diffusion in zoned magma chambers. *Contrib. Mineral. Petr.* **104**, 407–423.

Barnes V. E. (1940) North American tektites. *Univ. Texas Publ.* **3945**, pp. 477–582.

Barnes V. E. (1958) Properties of tektites pertinent to their origin. *Geochim. Cosmochim. Acta* **14**, 267–278.

Barnes V. E. (1964) Variation of petrographic and chemical characteristics of indochinite tektites within their strewn-field. *Geochim. Cosmochim. Acta* **28**, 893–913.

Barnes V. E. and Pitakpaivan K. (1962) Origin of Indochinite Tektites. *P. Natl. Acad. Sci.* **48**, 947–955.

Behrens H., Zhang Y. and Xu Z. (2004) H2O diffusion in dacitic and andesitic melts. *Geochim. Cosmochim. Acta* **68**, 5139–5150.

Behrens H., Zhang Y., Leschik M., Wiedenbeck M., Heide G. and Frischat G. H. (2007) Molecular H2O as carrier for oxygen diffusion in hydrous silicate melts. *Earth Planet. Sc. Lett.* **254**, 69–76.

Chapman D. R. and Scheiber L. C. (1969) Chemical investigation of Australasian tektites. *J. Geophys. Res.* **74**, 6737–6776.

Collins G. S., Melosh H. J. and Osinski G. R. (2012) The Impact-Cratering Process. *Elements* **8**, 25–30.

Cooper A. R. (1968) The use and limitations of the concept of an effective binary diffusion coefficient for multicomponent diffusion. In *Mass Transport in Oxides* (eds. J. B. Wachman and Franklin, A. D.). National Bureau of Standards Special Publication. pp. 79–84.

Crank J. (1975) *The Mathematics of Diffusion: 2d Ed*., Clarendon Press.

Delaney J. R. and Karsten J. L. (1981) Ion microprobe studies of water in silicate melts. Concentration-dependent water diffusion in obsidian. *Earth Planet. Sc. Lett.* **52**, 191–202.

Fisk M. R. (1986) Basalt magma interaction with harzburgite and the formation of high-magnesium andesites. *Geophys. Res. Lett.* **13**, 467–470.

French B. M. (1998) *Traces of Catastrophe: A Handbook of Shock-Metamorphic Effects in Terrestrial Meteorite Impact Structures*. Lunar and Planetary Institute, Houston, 120.

Gault D. E., Quaide W. L., Oberbeck V. R., French B. M. and Short N. M. (1968) Shock Metamorphism of Natural Materials (eds B. M. French and N. M. Short). Mono Book Corporation, pp. 87-99

Giuli G., Eeckhout S. G., Cicconi M. R., Koeberl C., Pratesi G. and Paris E. (2010) Iron oxidation state and local structure in North American tektites. *Geol. S. Am. S.* **465**, 645–651.

Glass B. P. (1990) Tektites and microtektites: key facts and inferences. *Tectonophysics* **171**, 393–404.

Grieve R. A. F. (1980) Impact bombardment and its role in proto-continental growth on the early earth. *Precambrian Res.* **10**, 217–247.

Grieve R. A. F. (1987) Terrestrial Impact Structures. *Annu. Rev. Earth Pl. Sc.* **15**.

Guo C. and Zhang Y. (2016) Multicomponent diffusion in silicate melts: SiO2–TiO2–Al2O3–MgO–CaO–Na2O–K2O System. *Geochim. Cosmochim. Acta* **195**, 126–141.

Guo C. and Zhang Y. (2018) Multicomponent diffusion in basaltic melts at 1350 °C. *Geochim. Cosmochim. Acta* **228**, 190–204.

Hauri E. H., Gaetani G. A. and Green T. H. (2006) Partitioning of water during melting of the Earth's upper mantle at H2O-undersaturated conditions. *Earth Planet. Sc. Lett.* **248**, 715–734.

Heaney P. J. (1994) Structure and chemistry of the low-pressure silica polymorphs. *Rev. Mineral. Geochem.* **29**, 1–40.

Heide K., Heide G. and Kloess G. (2001) Glass chemistry of tektites. *Planet. Space Sci.* **49**, 839–844.

Howard K. T. (2011) Volatile enhanced dispersal of high velocity impact melts and the origin of tektites. *P. Geologist. Assoc.* **122**, 363–382.

Humayun M. and Koeberl C. (2004) Potassium isotopic composition of Australasian tektites. *Meteorit. Planet. Sci.* **39**, 1509–1516.

Johnson B. C. and Melosh H. J. (2014) Formation of melt droplets, melt fragments, and accretionary impact lapilli during a hypervelocity impact. *Icarus* **228**, 347–363.

King E. A. (1977) The Origin of Tektites: A Brief Review: Pieces of the Moon? Some researchers thought so, but the lunar samples have completely dismissed this claim. *Am. Sci.* **65**, 212–218.

Kinnunen K. A. (1990) Lechatelierite inclusions in indochinites and the origin of tektites. *Meteoritics* **25**, 181–184.

Koeberl C. (1986) Geochemistry of Tektites and Impact Glasses. *Annu. Rev. Earth Pl. Sc.* **14**, 323–350.

Koeberl C. (1990) The geochemistry of tektites: an overview. *Tectonophysics* **171**, 405–422.

Koeberl C. (1992) Geochemistry and origin of Muong Nong-type tektites. *Geochim. Cosmochim. Acta* **56**, 1033–1064.

Koeberl C. (1994) Tektite origin by hypervelocity asteroidal or cometary impact: Target rocks, source craters, and mechanisms. In *Large Meteorite Impacts and Planetary Evolution* (eds. B. O. Dressier, Grieve, R.A.F., and Sharpton, V. L.). Geol. S. Am. S. Boulder, Colorado. pp. 133–151.

Koyaguchi T. (1989) Chemical gradient at diffusive interfaces in magma chambers. *Contrib. Mineral. Petr.* **103**, 143–152.

Lacroix A. (1915) La silice foudre considerée comme minéral (Lechatelierite). *B. Soc. Fr. Minéral.* **38**, 182.

Laporte D., Toplis M. J., Seyler M. and Devidal J.-L. (2004) A new experimental technique for extracting liquids from peridotite at very low degrees of melting: application to partial melting of depleted peridotite. *Contrib. Mineral. Petr.* **146**, 463–484.

Lesher C. E. and Walker D. (1986) Solution properties of silicate liquids from thermal diffusion experiments. *Geochim. Cosmochim. Acta* **50**, 1397–1411.

Mackenzie J. D. (1960) Fusion of Quartz and Cristobalite. *J. Am. Ceram. Soc.* **43**, 615–619.

Macris C. A., Turley R. J., Eiler J. M. and Stolper E. M. (2017) Using diffusion in tektites and experiments to investigate impact plume dynamics. Geological Society of America *Abstracts with Programs* **49** #208-4(abstr.).

Médard E., McCammon C. A., Barr J. A. and Grove T. L. (2008) Oxygen fugacity, temperature reproducibility, and H2O contents of nominally anhydrous piston-cylinder experiments using graphite capsules. *Am. Mineral.* **93**, 1838–1844.

Melosh H. J. (1989) *Impact cratering: A geologic process.* Oxford University Press, New York.

Melosh H. J. and Artemieva N. (2004) How Does Tektite Glass Lose Its Water? *Lunar Planet. Sci. XXXV* Lunar Planet. Inst., Houston. pp. 1723(abstr.).

Moore C. B., Canepa J. A. and Lewis C. F. (1984) Volatile non-metallic elements in tektites. *J. Non-Cryst. Solids* **67**, 345–348.

Mungall J. E. and Dingwell D. B. (1997) Actinide diffusion in a haplogranitic melt: Effects of temperature, water content, and pressure. *Geochim. Cosmochim. Acta* **61**, 2237–2246.

Newman S., Beckett J., Bashir N. and Stolper E. (1995) Water in an Indochinite: Implications for the Thermal History of Tektites. *Lunar Planet. Sci. XXVI.* Lunar Planet. Inst., Houston. pp. 1039-1040(abstr.).

Ni H., Behrens H. and Zhang Y. (2009) Water diffusion in dacitic melt. *Geochim. Cosmochim. Acta* **73**, 3642–3655.

O'Keefe J. A. (1976) Tektites and their origin. Elsevier Scientific Publishing Company, Amsterdam, Netherlands, pp. 266 (ISBN 0-44441-350-2).

O'Keefe J. D. and Ahrens T. J. (1993) Planetary cratering mechanics. *J. Geophys. Res.* **98**, 17011–17028.

Osinski G. R., Grieve R. A. F., Marion C. and Chanou A. (2012) Impact Melting. In *Impact Cratering* (eds. G.R. Osinski and E. Pierazzo) Wiley-Blackwell. pp. 125–145.

Osinski G. R. and Pierazzo E. (2012) *Impact Cratering: Processes and Products*., John Wiley & Sons.

Pack A., Kremer K., Albrecht N., Simon K. and Kronz A. (2010) Description of an aerodynamic levitation apparatus with applications in Earth sciences. *Geochem. T.* **11**, 4.

Pasek M. A., Block K. and Pasek V. (2012) Fulgurite morphology: a classification scheme and clues to formation. *Contrib. Mineral. Petr.* **164**, 477–492.

Persikov E. S. (1991) The Viscosity of Magmatic Liquids: Experiment, Generalized Patterns. A Model for Calculation and Prediction. Applications. In *Physical Chemistry of Magmas* Advances in Physical Geochemistry. Springer, New York, NY. pp. 1–40.

Richter F. M. (1993) A method for determining activity-composition relations using chemical diffusion in silicate melts. *Geochim. Cosmochim. Acta* **57**, 2019–2032.

Sato H. (1975) Diffusion coronas around quartz xenocrysts in andesite and basalt from Tertiary volcanic region in northeastern Shikoku, Japan. *Contrib. Mineral. Petr.* **50**, 49–64.

Schaller M. F., Fung M. K., Wright J. D., Katz M. E. and Kent D. V. (2016) Impact ejecta at the Paleocene-Eocene boundary. *Science* **354**, 225–229.

Simonson B. M. and Glass B. P. (2004) Spherule Layers—Records of Ancient Impacts. *Annu. Rev. Earth Pl. Sc.* **32**, 329–361.

Stöffler D. and Langenhorst F. (1994) Shock metamorphism of quartz in nature and experiment: I. Basic observation and theory*. *Meteoritics* **29**, 155–181.

Stöffler D., Artemieva N. A. and Pierazzo E. (2002) Modeling the Ries-Steinheim impact event and the formation of the moldavite strewn field. *Meteorit. Planet. Sci.* **37**, 1893–1907.

Trial A. F. and Spera F. J. (1994) Measuring the multicomponent diffusion matrix: Experimental design and data analysis for silicate melts. *Geochim. Cosmochim. Acta* **58**, 3769–3783.

Watson E. B. (1982) Basalt contamination by continental crust: Some experiments and models. *Contrib. Mineral. Petr.* **80**, 73–87.

Wilding M., Webb S. and Dingwell D. B. (1996) Tektite cooling rates: Calorimetric relaxation geospeedometry applied to a natural glass. *Geochim. Cosmochim. Acta* **60**, 1099–1103.

Xu Z. and Zhang Y. (2002) Quench rates in air, water, and liquid nitrogen, and inference of temperature in volcanic eruption columns. *Earth Planet. Sc. Lett.* **200**, 315–330.

Yu Y., Zhang Y. and Yang Y. (2015) Diffusion of SiO2 in Rhyolitic Melt. *AGU Fall Meeting Abstracts* **41**, V41B-3070(abstr.).

Zhang Y. (1993) A modified effective binary diffusion model. *J. Geophys. Res.-Sol. Ea.* **98**, 11901–11920.

Zhang Y. (2008) *Geochemical kinetics*., Princeton University Press.

Zhang Y. (2010) Diffusion in Minerals and Melts: Theoretical Background. *Rev. Mineral. Geochem.* **72**, 5–59.

Zhang Y., Walker D. and Lesher C. E. (1989) Diffusive crystal dissolution. *Contrib. Mineral. Petr.* **102**, 492–513.

Zhang Y., Ni H. and Chen Y. (2010) Diffusion Data in Silicate Melts. *Rev. Mineral. Geochem.* **72**, 311–408.

Figure Captions

Figure 1. Indochinite tektite LTS1 used in this study. (**a**) Photograph of LTS1 showing its splash-form morphology and orientation of sectioning perpendicular to the long axis. (**b**) Transmitted light photomicrograph of a section of LTS1 showing the presence of vesicles, schlieren (flow bands of relatively high SiO_2 glass), and lechatelierite (>99% SiO_2 glass inclusions) surrounded by a matrix of peraluminous felsic host glass.

Figure 2. Back-scattered electron images of lechatelierite (dark grey regions with vesicles) and surrounding felsic glass in indochinite LTS1 showing variations in size, shape, and vesicularity. Scale bars are 100 μm for all panels. Relative greyscale variations between panels are not meaningful, but darker grey regions in a single panel indicate higher silica content. Features of interest discussed in the text are labeled with capital letters ([A], [B], etc.) and indicated with arrows. [A] – vesicles adjacent to lechatelierite; [B] – vesicles inside lechatelierite; [C] – lower SiO_2 regions within lechatelierite; [D] – rounded, convex outward lechatelierite boundaries; [E] – irregular embayments or cusps in lechatelierite boundaries, likely reflecting deformation of the

boundaries by growing vesicles; and [F] – diffuse intermediate grey haloes surrounding lechatelierite.

Figure 3. Typical concentration profiles of major elements across the boundary between lechatelierite and the surrounding felsic glass in a natural tektite: Panel (**a**) shows a back-scattered electron image of a lechatelierite inclusion (dark grey) in tektite LTS1 surrounded by a diffusion halo that separates the lechatelierite from the far-field, lighter grey felsic glass (same as Fig. 2e of this study); (**b**) and (**c**) show concentration profiles along the A-B traverse (note the difference in vertical scale between (**b**) and (**c**)). Light grey shaded regions in (**b**) and (**c**) indicate points inside of the lechatelierite. Unshaded regions where the concentration profiles are changing represent the portions of the diffusion halo on either side of the lechatelierite. Where the concentrations level out (stop changing), the far-field felsic matrix glass has been reached.

Figure 4. Oxide profiles across the lechatelierite-host glass boundary from Fig. 3 (right side), normalized to a 0-1 scale for direct comparison of profile topologies. The concentration profiles separating the lechatelierite and the far-field felsic glass are of similar extent for all oxides shown here; the profiles are asymmetric, becoming steeper as the lechatelierite inclusion is approached (as described in the text, this is indicative of compositionally dependent diffusion coefficients, with the D's for all elements decreasing with increasing concentration of SiO_2); the steepness of the profiles within ~10 μm of the "edge" of the lechatelierite for the oxides other than SiO_2 is variable, but the order is systematic (K > Na > Al ~ Ti > Fe > Ca ~ Mg) and similar for all measured profiles; and K has a maximum in concentration in the boundary layer,

indicating that it diffused uphill (i.e., against its own concentration gradient) in this region of the boundary layer.

Figure 5. Variation diagrams showing compositional variation of major oxides and alkalis vs. SiO_2 for seven traverses across lechatelierite into the felsic matrix glass in tektite LTS1.

Figure 6. Back-scattered electron images of levitation laser experiments at 1800 °C from 1 (**a**) to 80 (**e**) seconds. Bright arcs in (**d**) and (**e**) are portions of the brass mounting plug. Note that the scales are not identical for all panels.

Figure 7. Back-scattered electron images of laser levitation experiments at 2000 °C from 5 (**a**) to 120 (**e**) seconds.

Figure 8. Back-scattered electron images of laser levitation experiments at 2200 °C from 5 (**a**) to 120 (**e**) seconds. Note that the scales are not identical for all panels.

Figure 9. Variation diagrams showing major element compositional variation vs. SiO_2 for analyses from experiments held at 1800, 2000, and 2200 °C for ~80 s (open colored symbols) and from traverses in the natural tektite (grey circles).

Figure 10. (**a**) BSE image of lechatelierite in experiment run at 2000 °C for 50 s. Red line (A-B) indicates EPMA traverse. (**b**) Oxide concentrations in wt % vs. distance along the traverse. (**c**)

Zoomed in version of (**b**) showing lower concentration oxides (including uphill diffusion of K_2O).

Figure 11. (**a**) Oxide concentration variation with distance away from the "edge" of the lechatelierite. Solid curves show data from the 2200° C, 50 s experiment. Open circles are data from natural tektite LTS1 (see Fig. 3). (**b**) Enlargement of (**a**) showing the correspondence between the natural and experimental samples for the low concentration oxides. Note that this correspondence extends to the region of uphill diffusion of K_2O in this experiment and reasonably well to the Na_2O profile despite alkali loss during the experiment

Figure 12. SiO_2 concentration (wt%) vs. distance in experiments heated to 2200 ℃ with run duration increasing from left to right from 1 s in to 80 s (run duration is indicated in the upper right corner of each panel). The profile in each panel extends from lechatelierite (left) to felsic host glass (right). The blue shaded regions (and the number at the lower right of this region in each panel) indicates the profile length, defined as the distance between points at 16 and 84% of the profile's height). Profile length increases with increases with the square root of time (see Fig. 13).

Figure 13. Plots of profile lengths in experiments (calculated as the distance between 16-84% of a given concentration profile's height) for SiO_2 (**a**) and Al_2O_3 (**b**) vs. the square root of the duration of the experiments at 1800 (red triangles), 2000 (blue circles), 2200 (black diamonds), and 2400 ℃ (green squares). Solid lines through data are best fits to each temperature series (constrained to go through the origin). Dashed horizontal line and grey band represent the

average profile length and associated 1σ error (SiO_2 = 19.1 ± 2.5 μm; Al_2O_3 = 18.9 ± 1.2 μm), obtained by averaging the SiO_2 and Al_2O_3 profile lengths of 7 boundaries measured in the natural tektite, LTS1 (Table 2). The angle at which the grain boundaries are cut in the tektite slabs likely plays a significant role in producing the observed scatter.

Figure 14. The diffusivities of (**a**) SiO_2, (**b**) Al_2O_3, (**c**) FeO, (**d**) MgO, and (**e**) CaO as determined from Eq. (2) and the slopes of the best fit lines in Fig. 13 and Fig. S9 for each temperature series, plotted as ln$D$ (m^2/s) versus $10^4/T$ (K^{-1}) (T (°C)) is also shown on upper horizontal axes). Activation energies (E_a) shown are calculated from Equation (3). As shown in (**f**), all oxides shown here have similar D values at all temperatures and similar slopes (note that the alkalis have been excluded due to the possible effects of alkali loss on interpretation of the results). All errors (ln$D$ and E_a) are 2σ. Error bars on figure are mostly smaller than symbols.

Figure 15. The BSE image (**a**) shows a lechatelierite (dark grey) from experiment ALLF 7, held at 2000 °C for 5 s. The red line indicates where an EPMA traverse (A-B) measured oxide concentration values starting inside of the lechatelierite (A), crossing the lechatelierite-felsic glass boundary zone, and ending in the felsic glass (B). Regions of unmelted quartz, lechatelierite, and felsic glass are indicated. Bright (white) areas are surface contamination and charging (not included in traverse). Plots showing the concentration of SiO_2 (wt%) (**b**) and Al2O3 (wt%) (**c**) vs. distance (μm) for the traverse from (A) to (B) in the BSE image (**a**). Closed symbols (circles) are EMPA data from the traverse, while the solid curve is fit using the Eq. (4). Further explanation in the text.

Figure 16. Arrhenius plot showing data from experimental studies by K89 (Koyaguchi, 1989) and W82 (Watson, 1982) at 55 wt% SiO_2 and from B90 (Baker, 1990) at 65 (open triangles), 70 (open circles), and 75 wt% SiO_2 (open squares). Diamond symbols are data from this study: pink diamonds represent diffusivities calculated using the interdiffusion profile lengths with Eq. (2) (this represents an average diffusivity); green and blue diamonds represent diffusivities calculated using Eq. (4), for 75 and 100 wt% SiO_2 respectively (this is why they have the same activation energy). 2σ error bars are smaller than symbols for most data points.

Figure 17. The exponential dependence of the diffusivity of SiO_2 on melt composition comparing results from this study with results based on experimental studies that measured the diffusion of SiO_2 between basalt and more felsic melts at 10 kbar, 1300-1500 °C (L&W86: Lesher and Walker, 1986; K89: Koyaguchi,1989) and between dacitic and rhyolitic melts at 1 atm, ~1200 to 1400 °C (B90: Baker, 1990). In each set of experiments, a logarithmic relationship was assumed, and these are the fits of their concentration profiles using this functional form.

Figure 18. Plot showing the family of possible temperature-time solutions estimated using the relationship between interdiffusion profile lengths of non-alkali oxides in our experiments at different temperatures and times, and the average profile length of the natural tektite, LTS1 (Figs. 13 and S9). At a given T, the profile length of each element in the boundary zone around a lechatelierite inclusion can be used to determine the isothermal heating time (t) required to produce the observed profile length (see first paragraph in §5.2 for further explanation and example). Each oxide has its own curve, but since the profile lengths and $\ln D$ vs. $10^4/T$ lines are essentially identical for all of the oxides studied (Fig. 14f), the permissible combinations of t and

T are similar regardless of the oxide chosen. However, lower temperature, longer time estimates show the largest range between oxides. According to these calculations, this Australasian tektite (LTS1) could have been entrained in an isothermal impact vapor plume at 2400, 2200, 2000, and 1800 °C for ~3, 25-33, 59-74, or 521-699 s, respectively.

Figure 19. Comparing data from natural tektite (open circles) with results of running a forward model using calculated D_{SiO_2} values calculated with Eq. (4) at 2000 and 2200 °C for 0-120 s (colored lines) are consistent with acceptable *T-t* conditions based on profile length method (Eq. (2)): ~66 s at 2000 °C and ~25 s at 2200 °C.

Figure 1

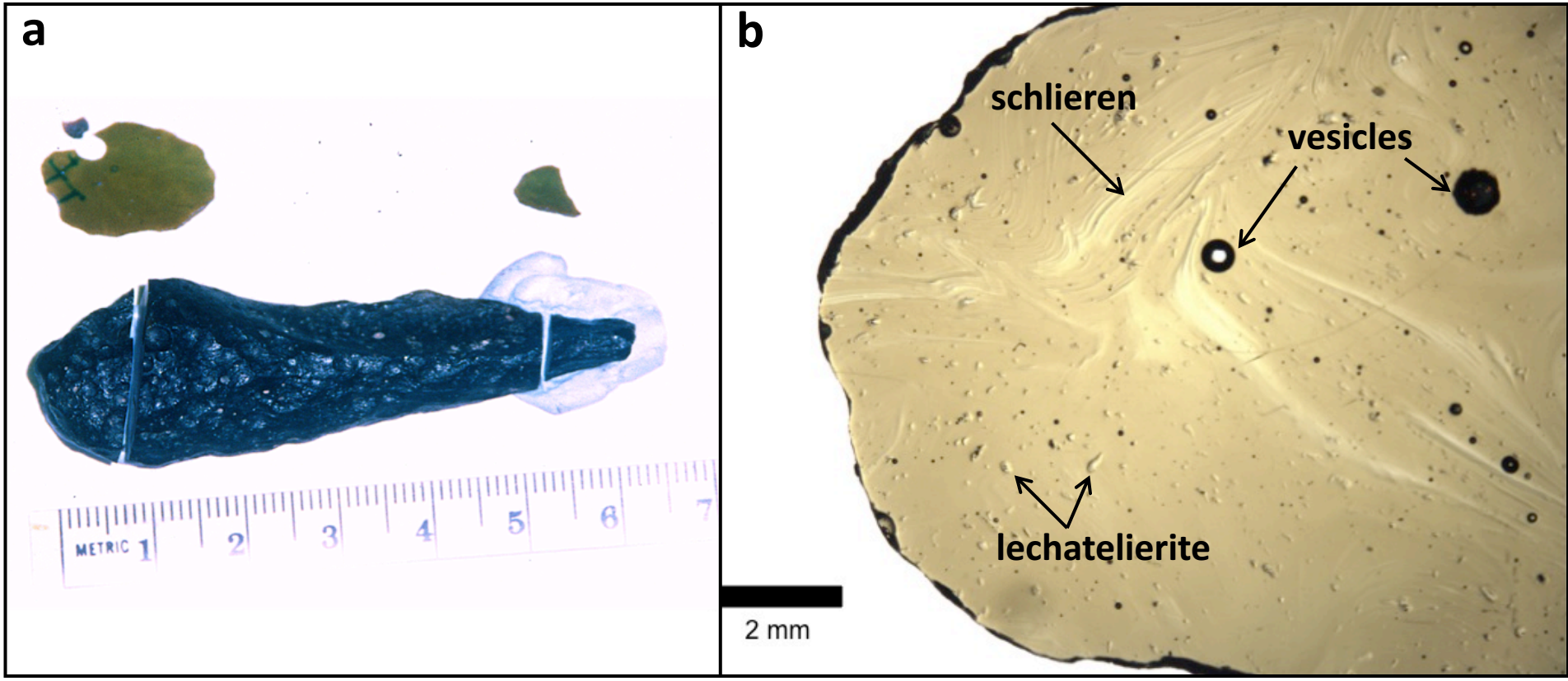

Fig. 1

Figure 2

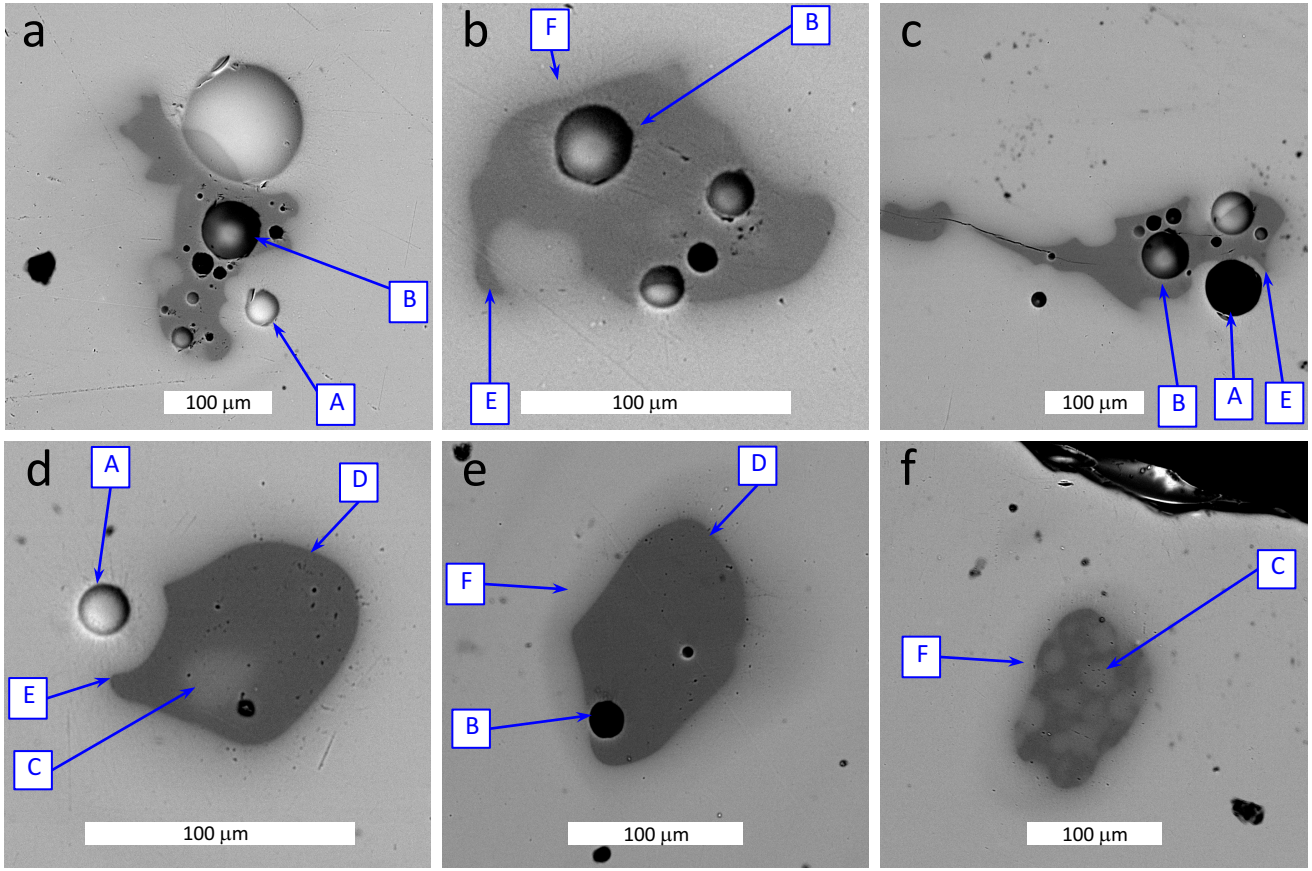

Fig. 2

Figure 3

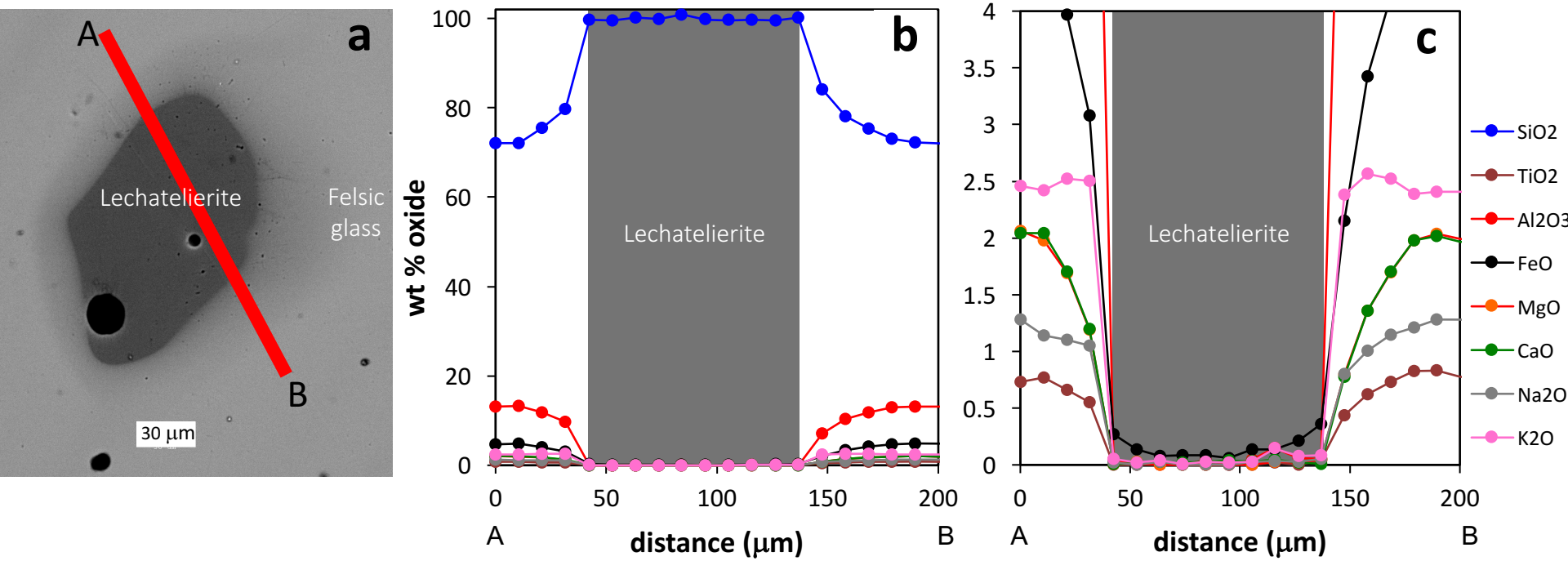

Fig. 3

Figure 4

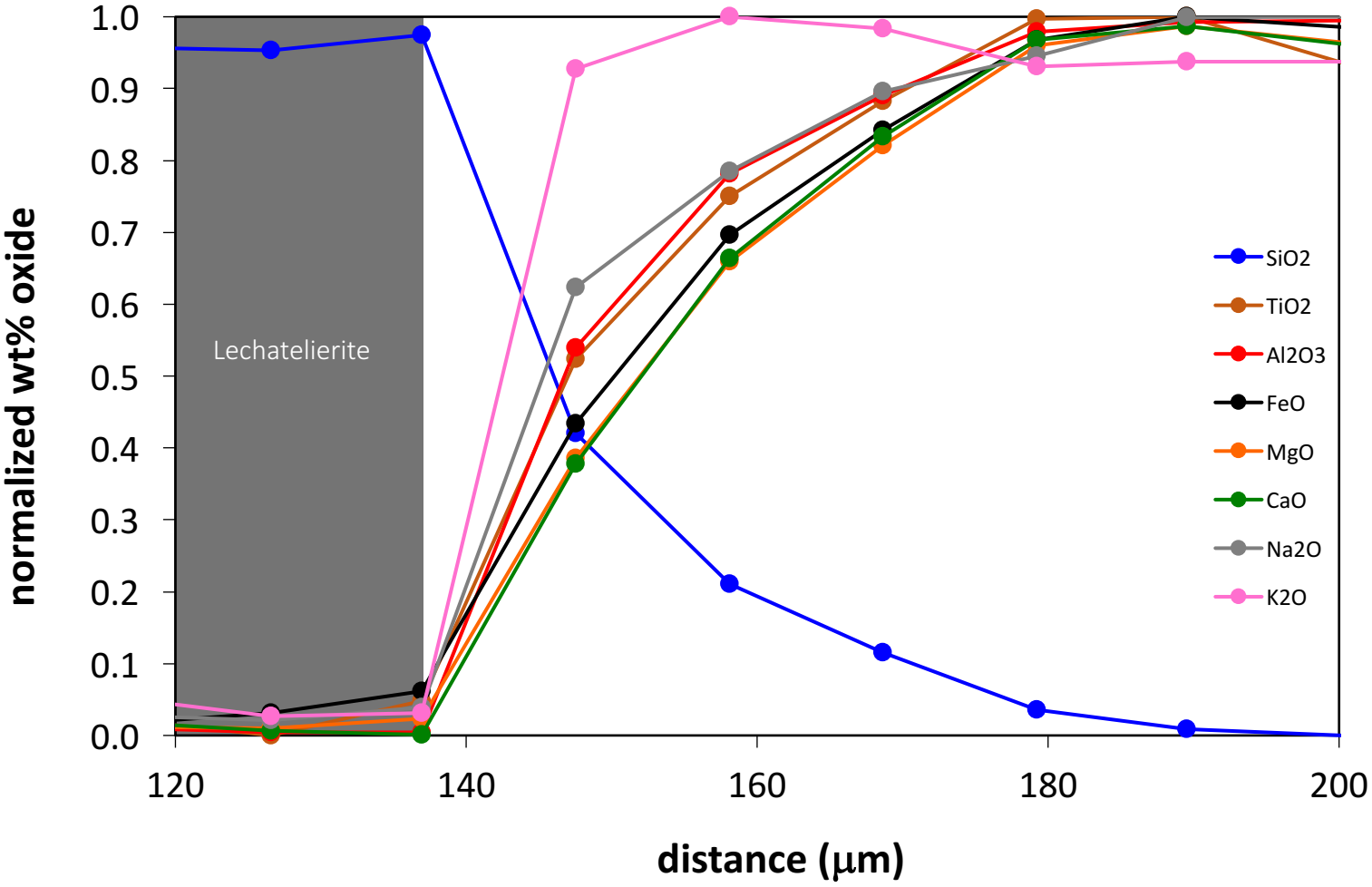

Fig. 4

Figure 5

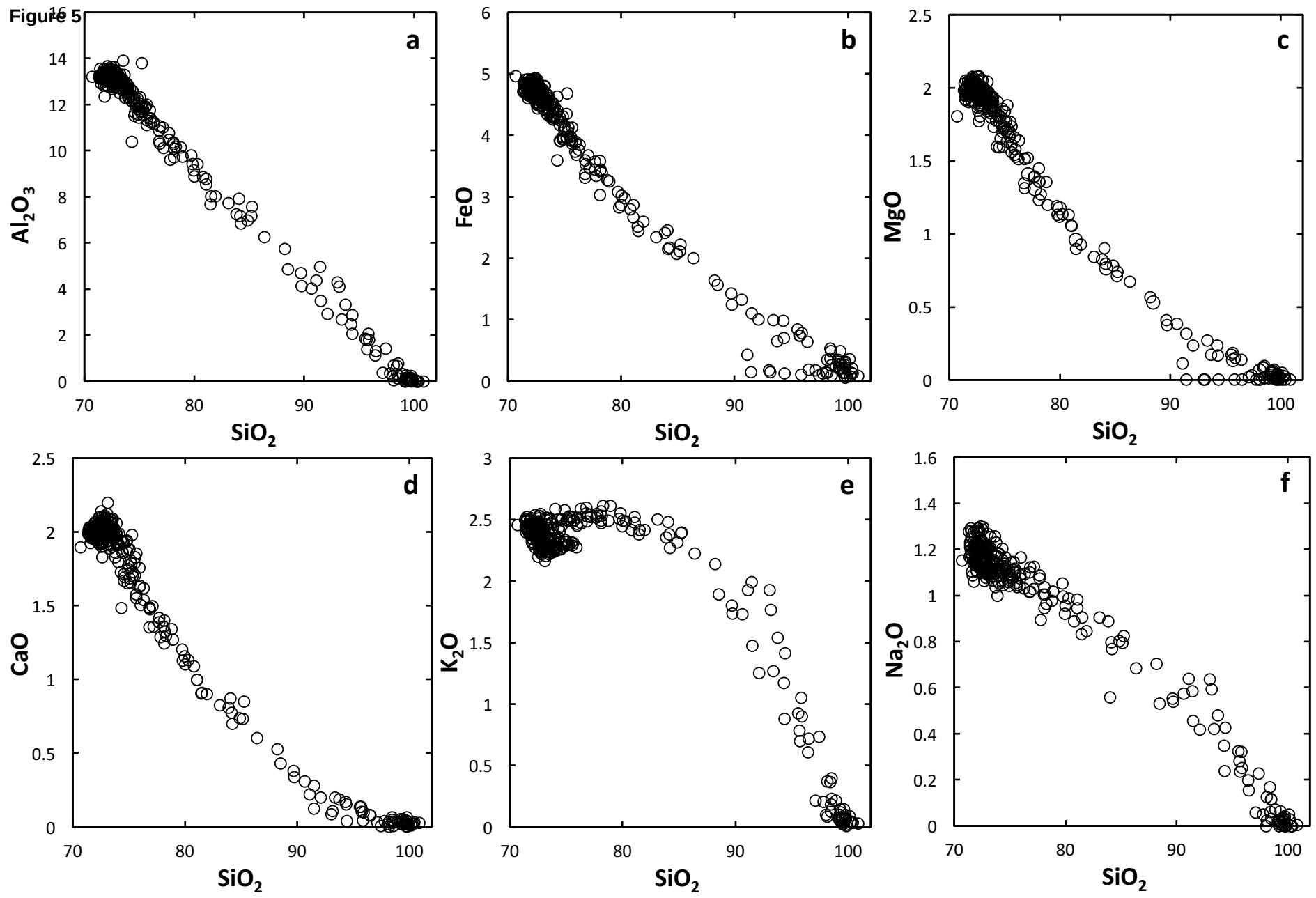

Fig. 5

Fig. 6

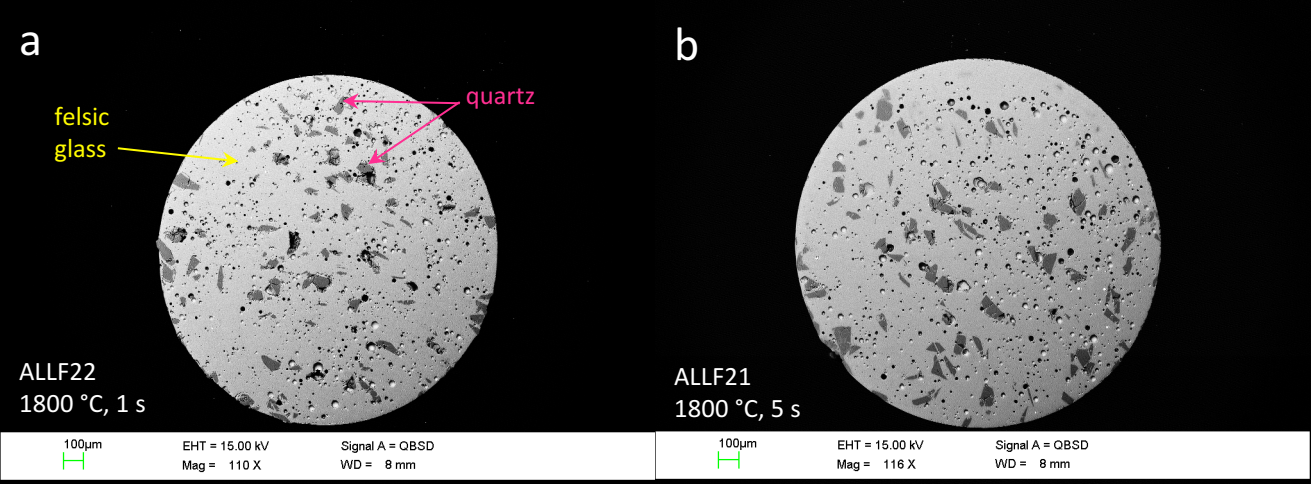
a
felsic glass
quartz
ALLF22
1800 °C, 1 s
100µm
EHT = 15.00 kV
Mag = 110 X
Signal A = QBSD
WD = 8 mm

b
ALLF21
1800 °C, 5 s
100µm
EHT = 15.00 kV
Mag = 116 X
Signal A = QBSD
WD = 8 mm

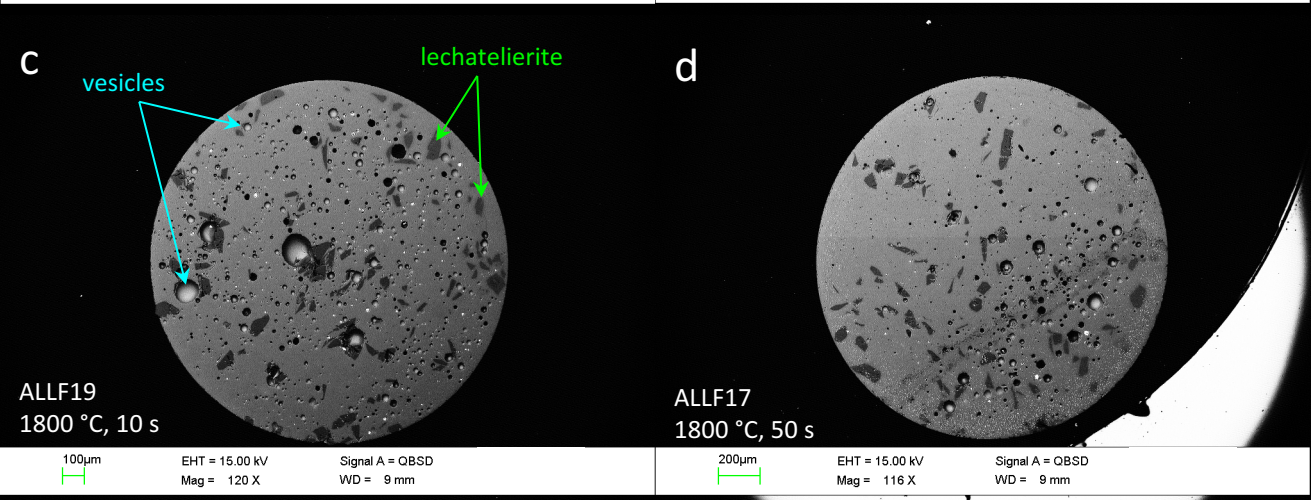
c
vesicles
lechatelierite
ALLF19
1800 °C, 10 s
100µm
EHT = 15.00 kV
Mag = 120 X
Signal A = QBSD
WD = 9 mm

d
ALLF17
1800 °C, 50 s
200µm
EHT = 15.00 kV
Mag = 116 X
Signal A = QBSD
WD = 9 mm

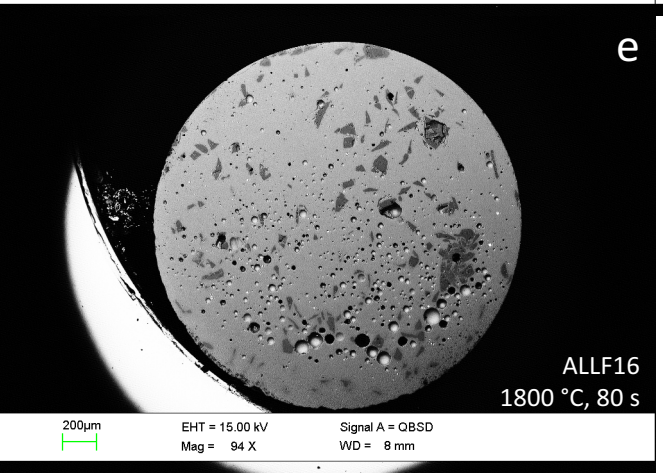
e
ALLF16
1800 °C, 80 s
200µm
EHT = 15.00 kV
Mag = 94 X
Signal A = QBSD
WD = 8 mm

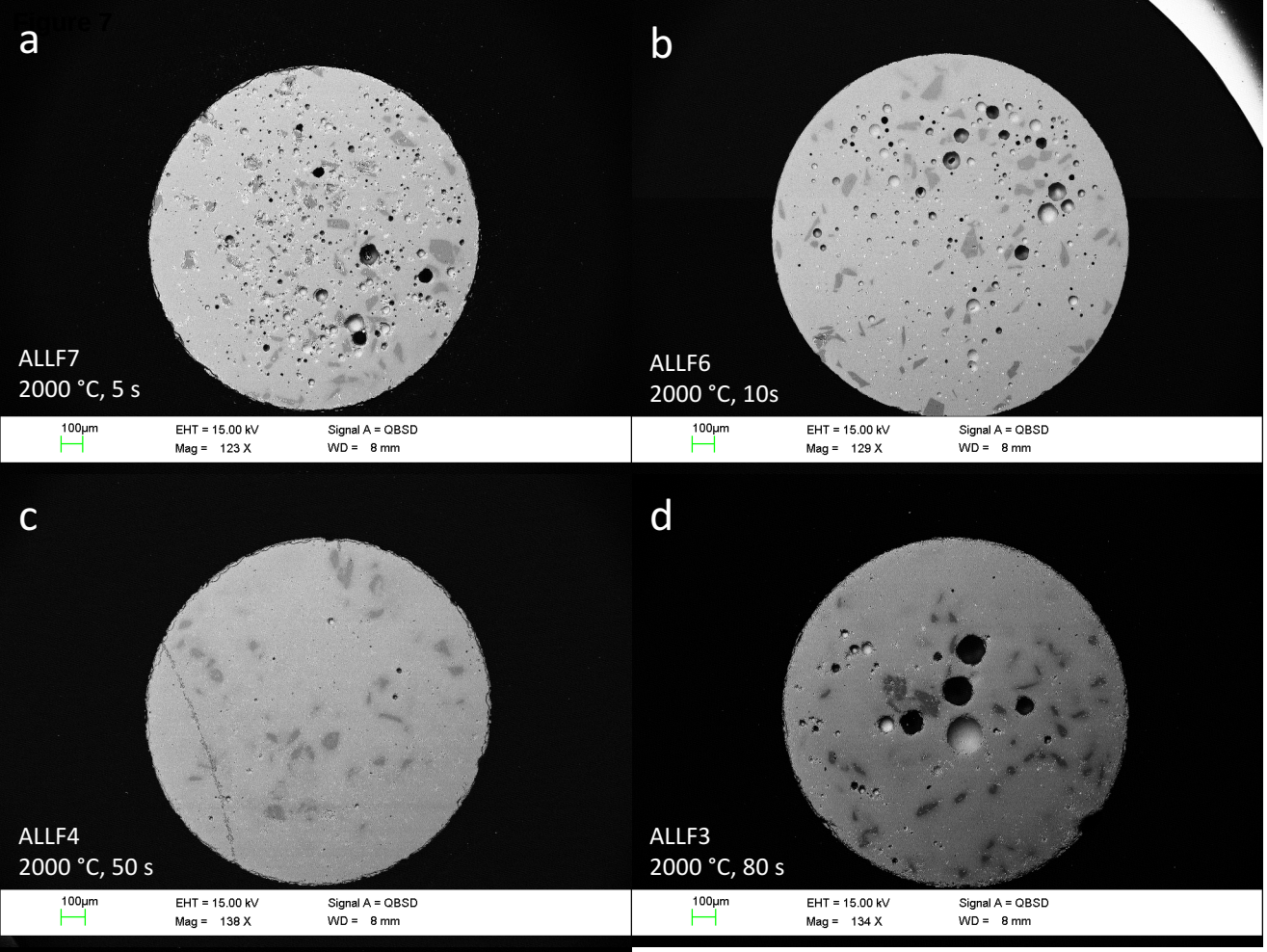
a
ALLF7
2000 °C, 5 s
100µm
EHT = 15.00 kV
Mag = 123 X
Signal A = QBSD
WD = 8 mm
b
ALLF6
2000 °C, 10s
100µm
EHT = 15.00 kV
Mag = 129 X
Signal A = QBSD
WD = 8 mm
c
ALLF4
2000 °C, 50 s
100µm
EHT = 15.00 kV
Mag = 138 X
Signal A = QBSD
WD = 8 mm
d
ALLF3
2000 °C, 80 s
100µm
EHT = 15.00 kV
Mag = 134 X
Signal A = QBSD
WD = 8 mm
e
ALLF2
2000 °C, 120s
100µm
EHT = 15.00 kV
Mag = 131 X
Signal A = QBSD
WD = 8 mm

Fig. 7

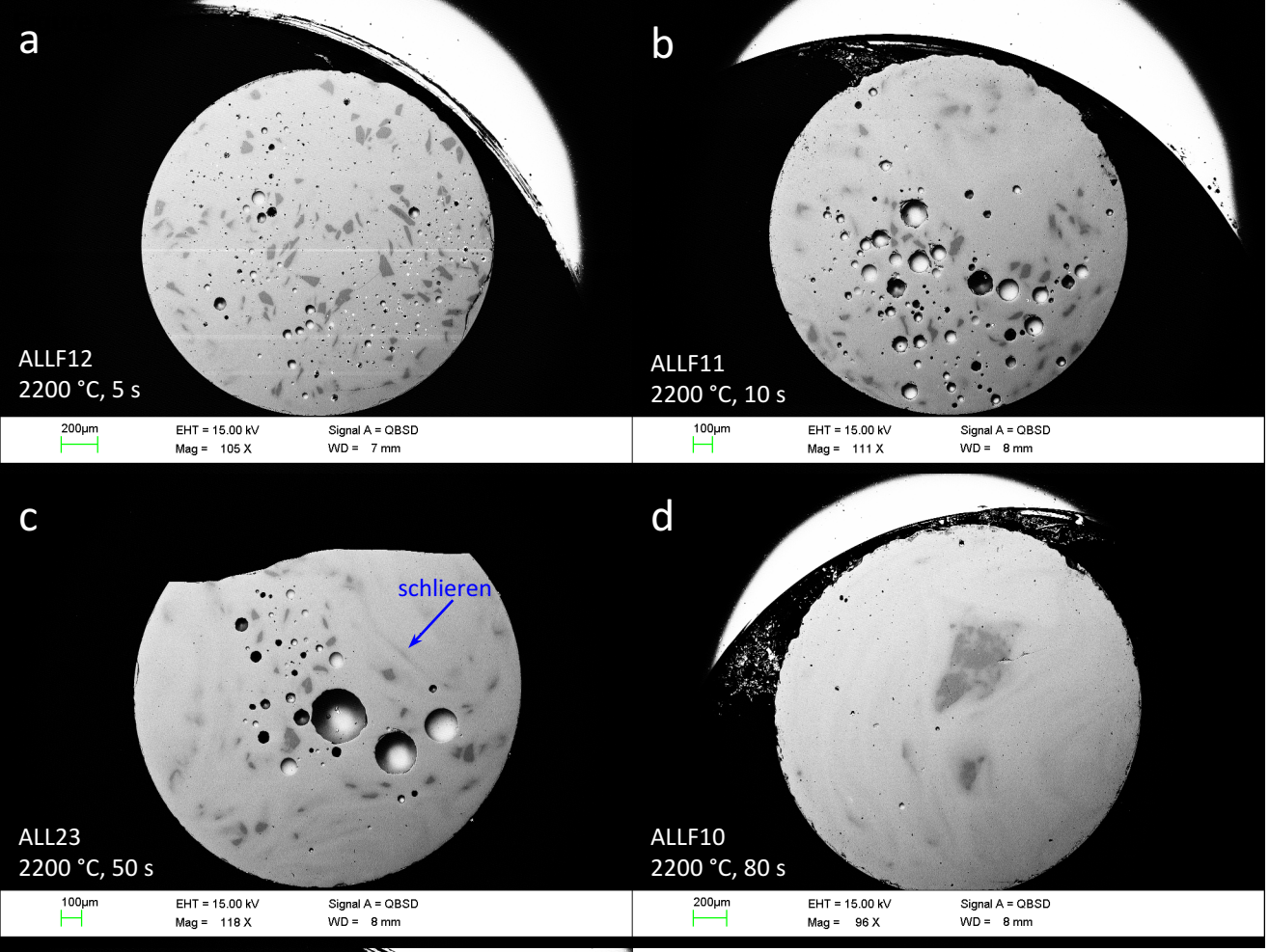
a
ALLF12
2200 °C, 5 s
200µm
EHT = 15.00 kV
Mag = 105 X
Signal A = QBSD
WD = 7 mm
b
ALLF11
2200 °C, 10 s
100µm
EHT = 15.00 kV
Mag = 111 X
Signal A = QBSD
WD = 8 mm
c
schlieren
ALL23
2200 °C, 50 s
100µm
EHT = 15.00 kV
Mag = 118 X
Signal A = QBSD
WD = 8 mm
d
ALLF10
2200 °C, 80 s
200µm
EHT = 15.00 kV
Mag = 96 X
Signal A = QBSD
WD = 8 mm
e
ALLF14
2200 °C, 120 s
100µm
EHT = 15.00 kV
Mag = 140 X
Signal A = QBSD
WD = 8 mm

Fig. 8

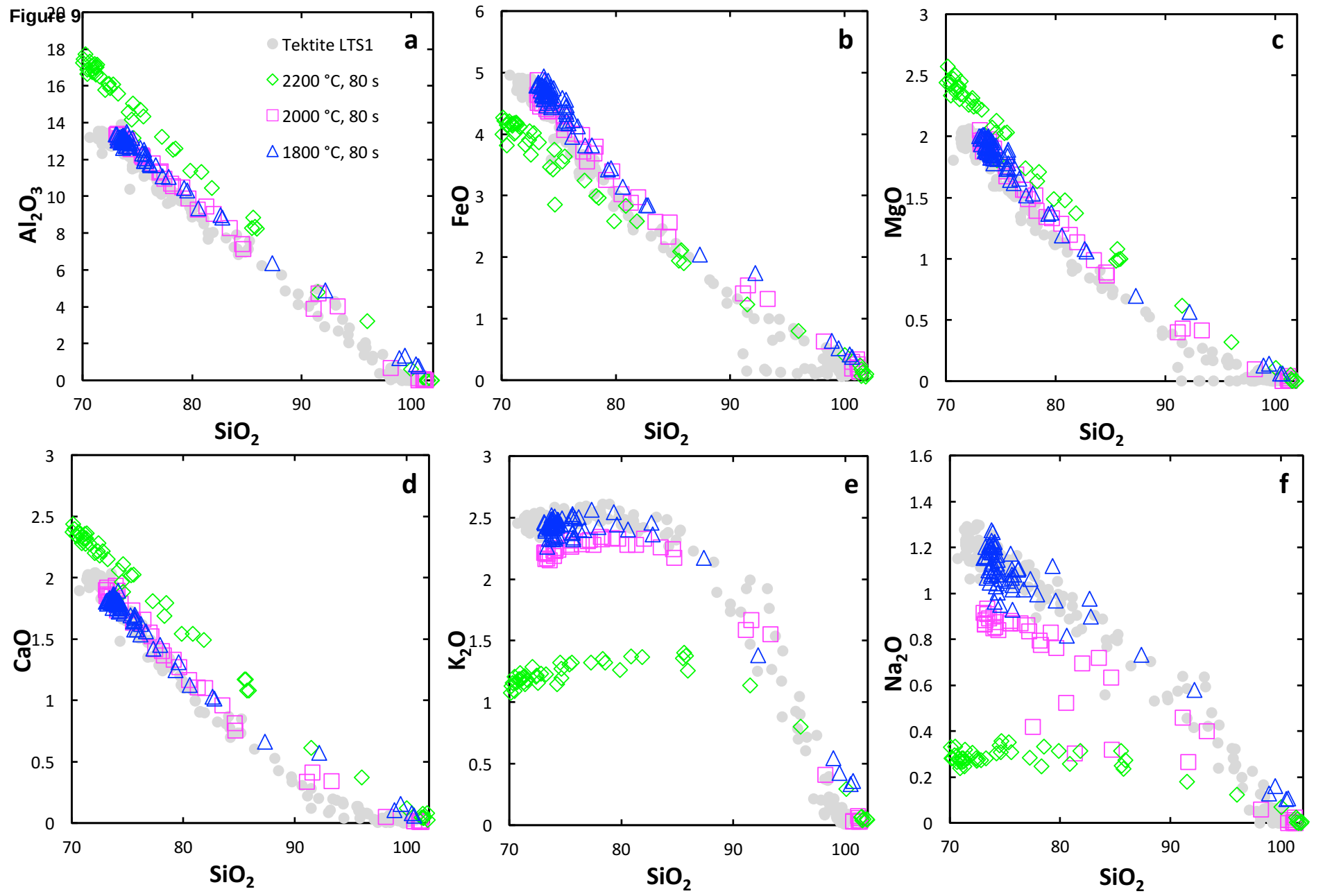
Figure 9
Tektite LTS1
2200 °C, 80 s
2000 °C, 80 s
1800 °C, 80 s
a
b
c
d
e
f
Al2O3
FeO
MgO
CaO
K2O
Na2O
SiO2

Fig. 9

Figure 10

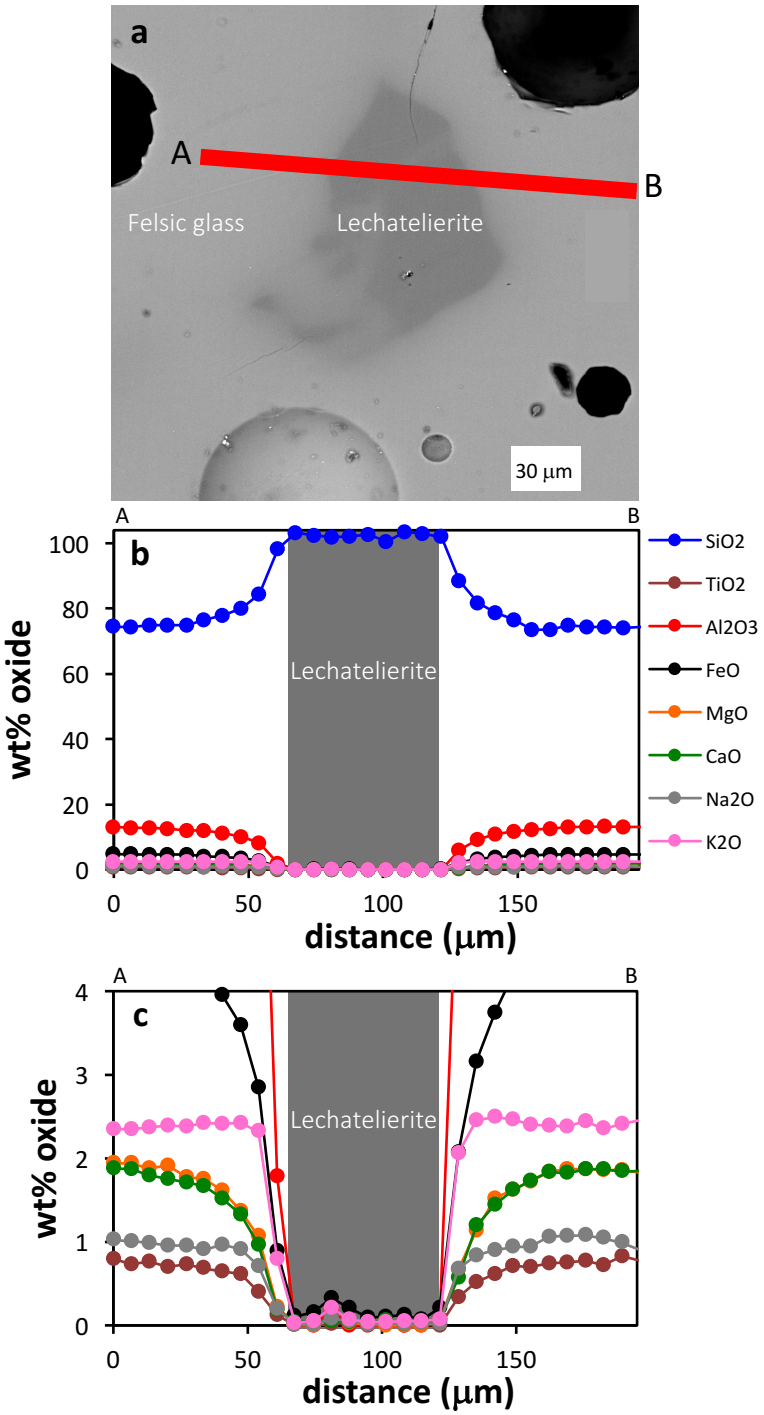

Fig. 10

Figure 11

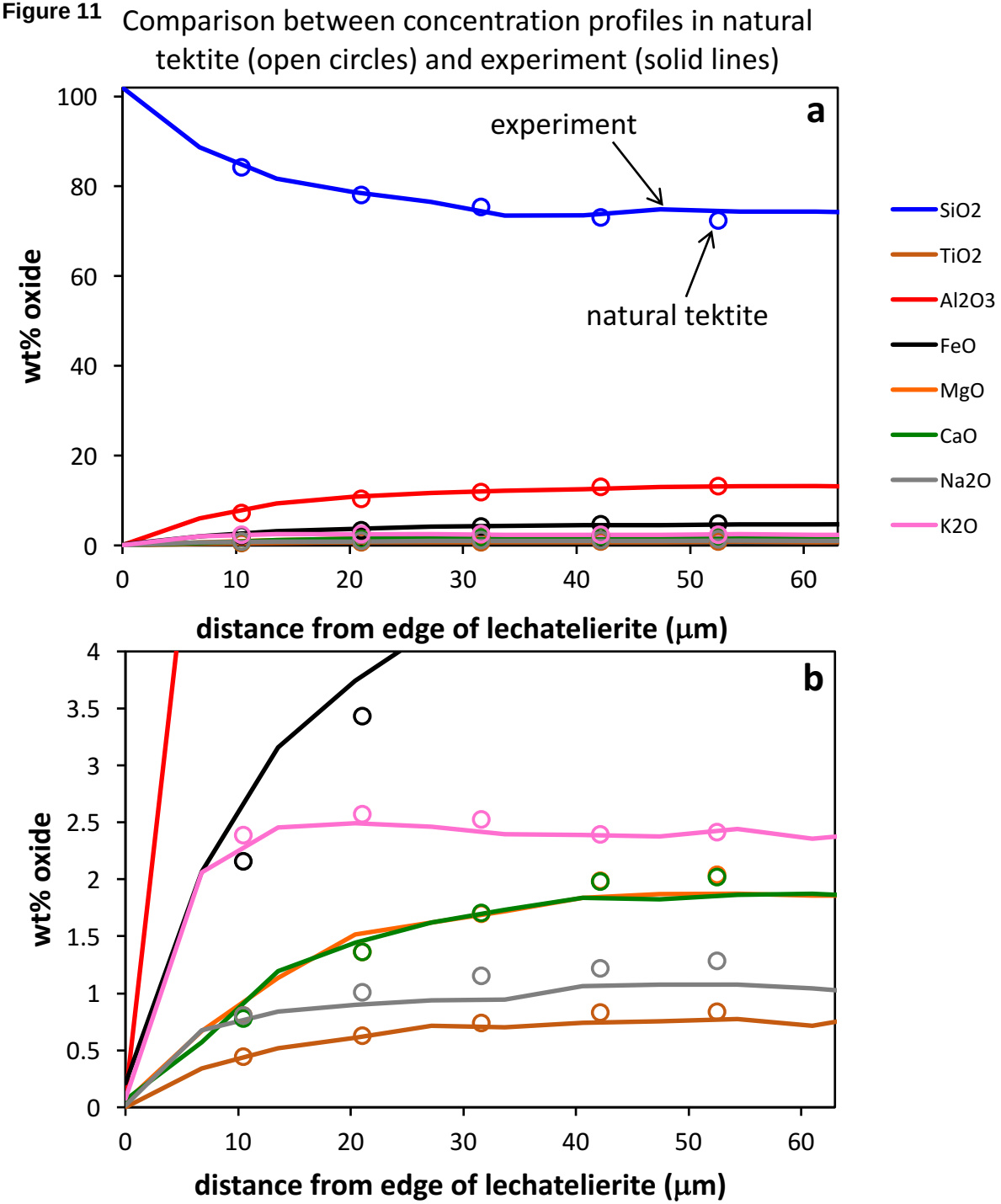

Fig. 11

Figure 12

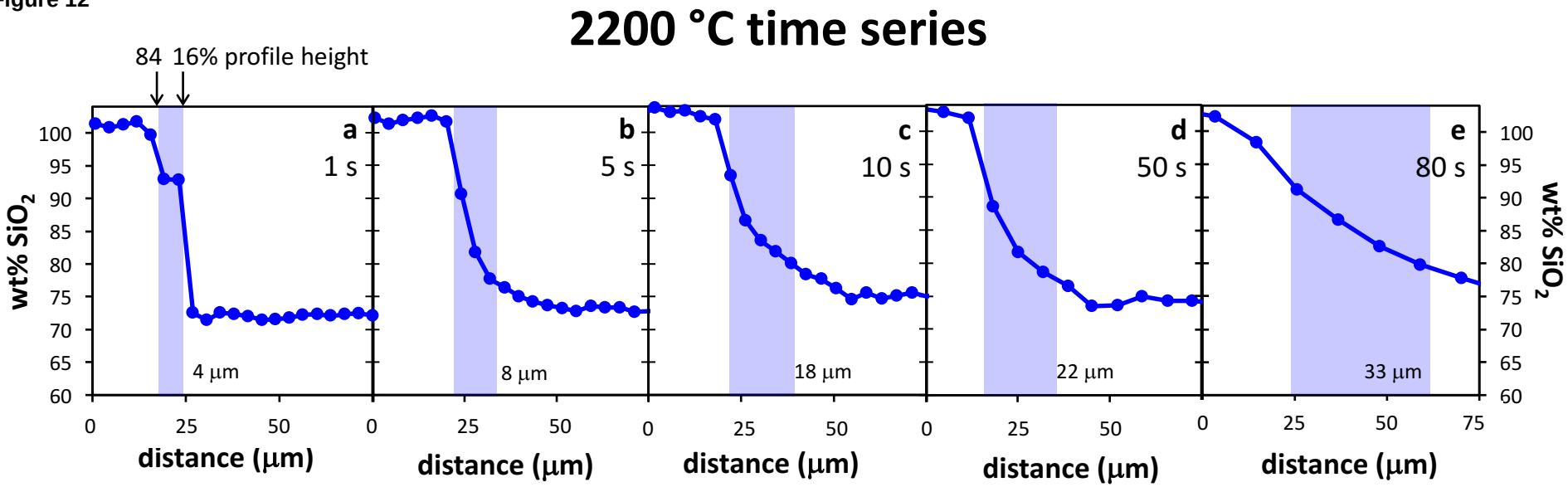

Fig. 11

Figure 13

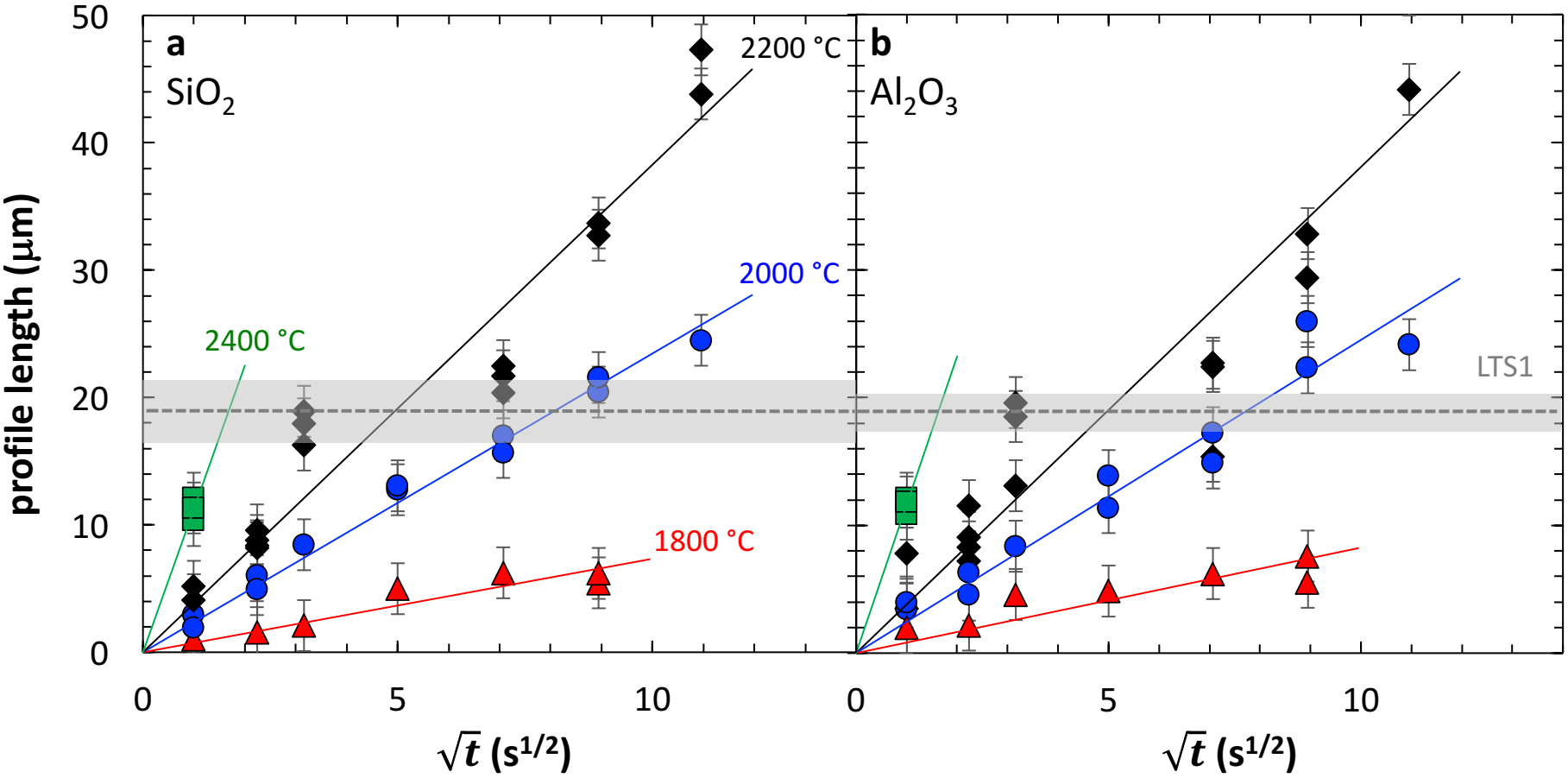

Fig. 13

Figure 14

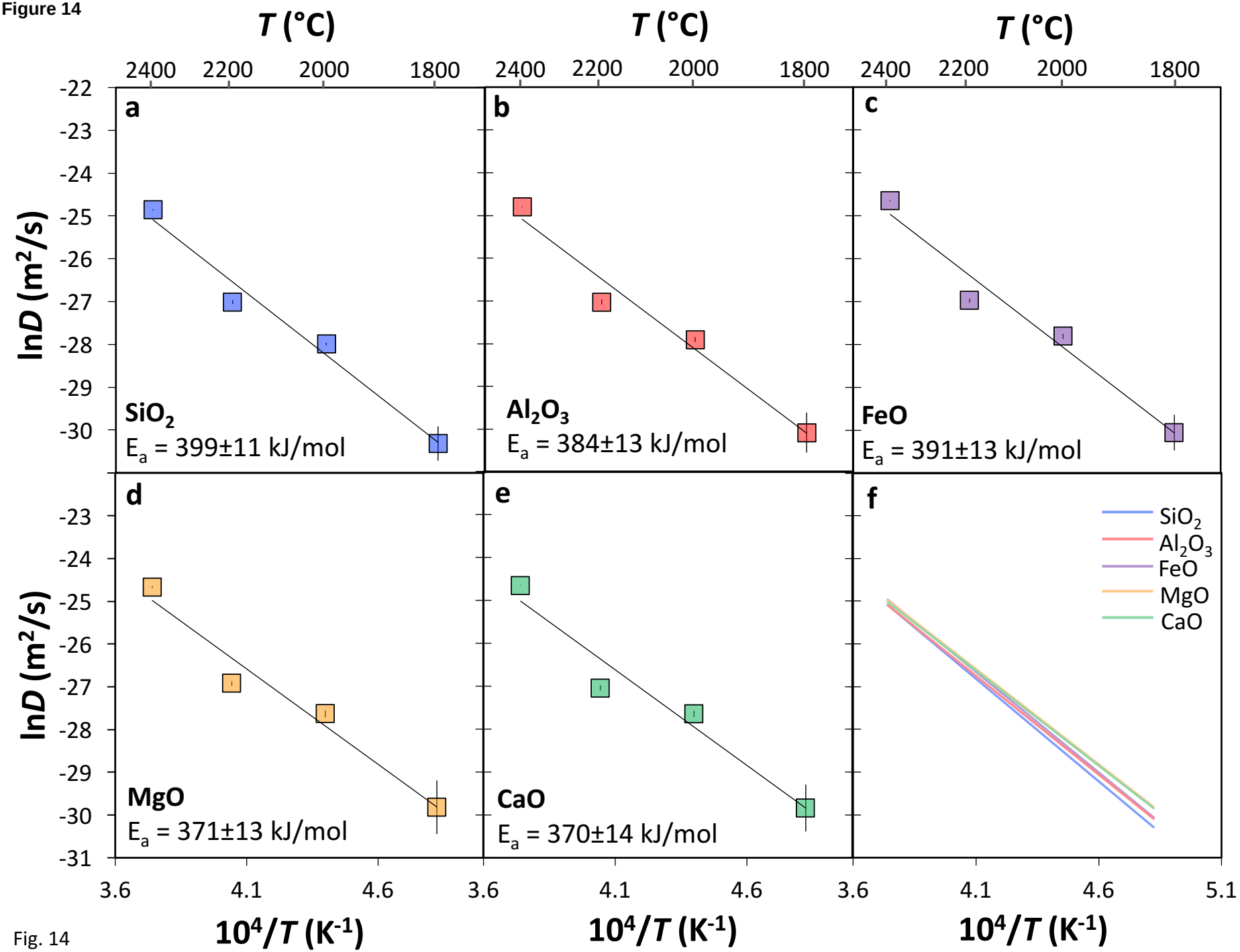

Fig. 14

Figure 15

Examples of the diffusion model presented in §5.1.2 (Eq. 4), applied to SiO_2 and Al_2O_3, for a traverse across the lechatelierite-felsic glass boundary from experiment ALLF 7.

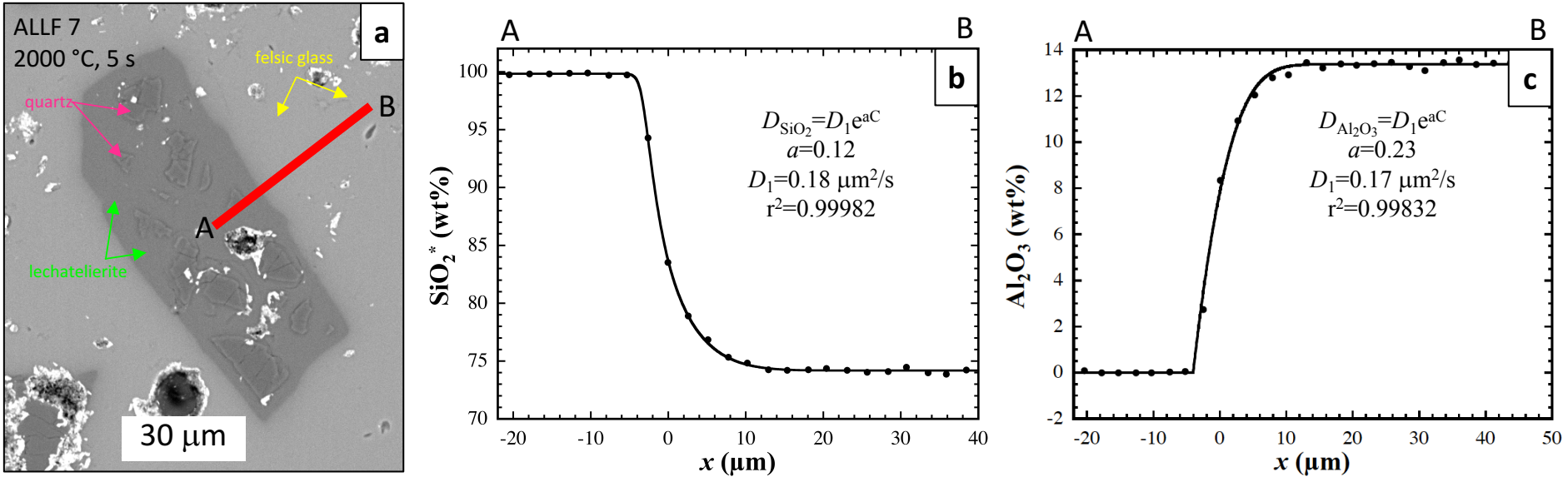

Fig. 15

Figure 16

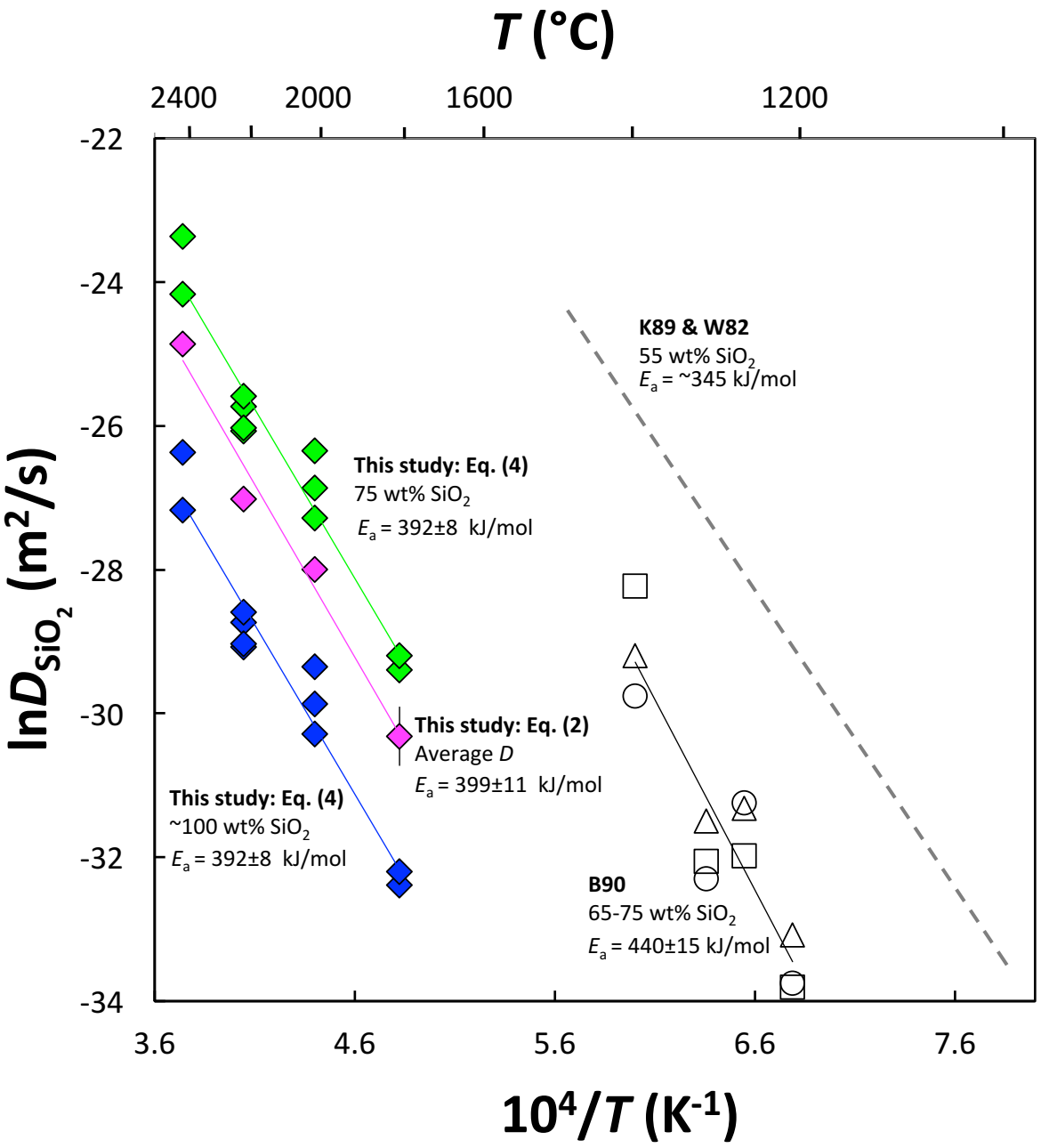

Fig. 16

Figure 17

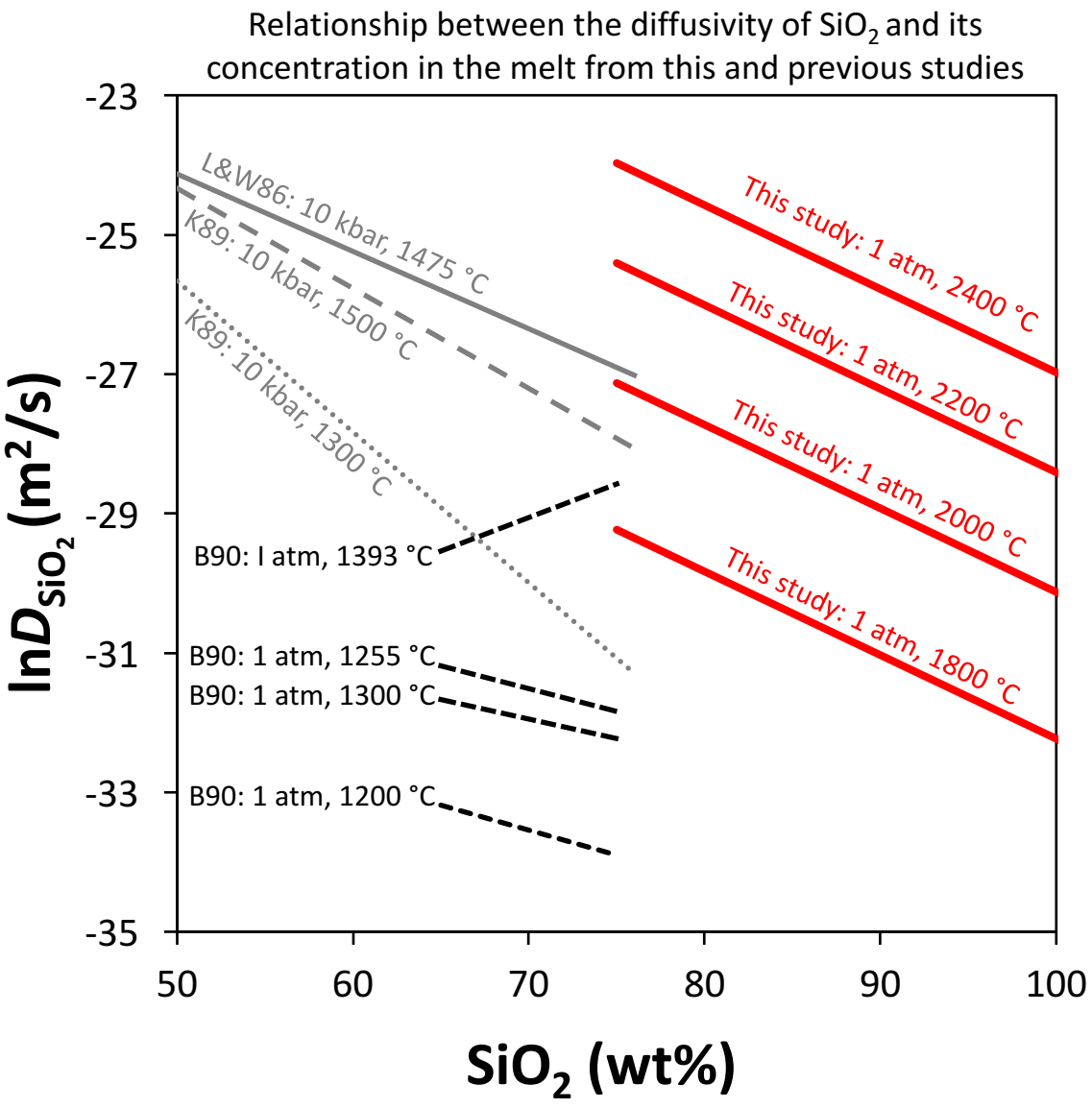

Fig. 17

Figure 18

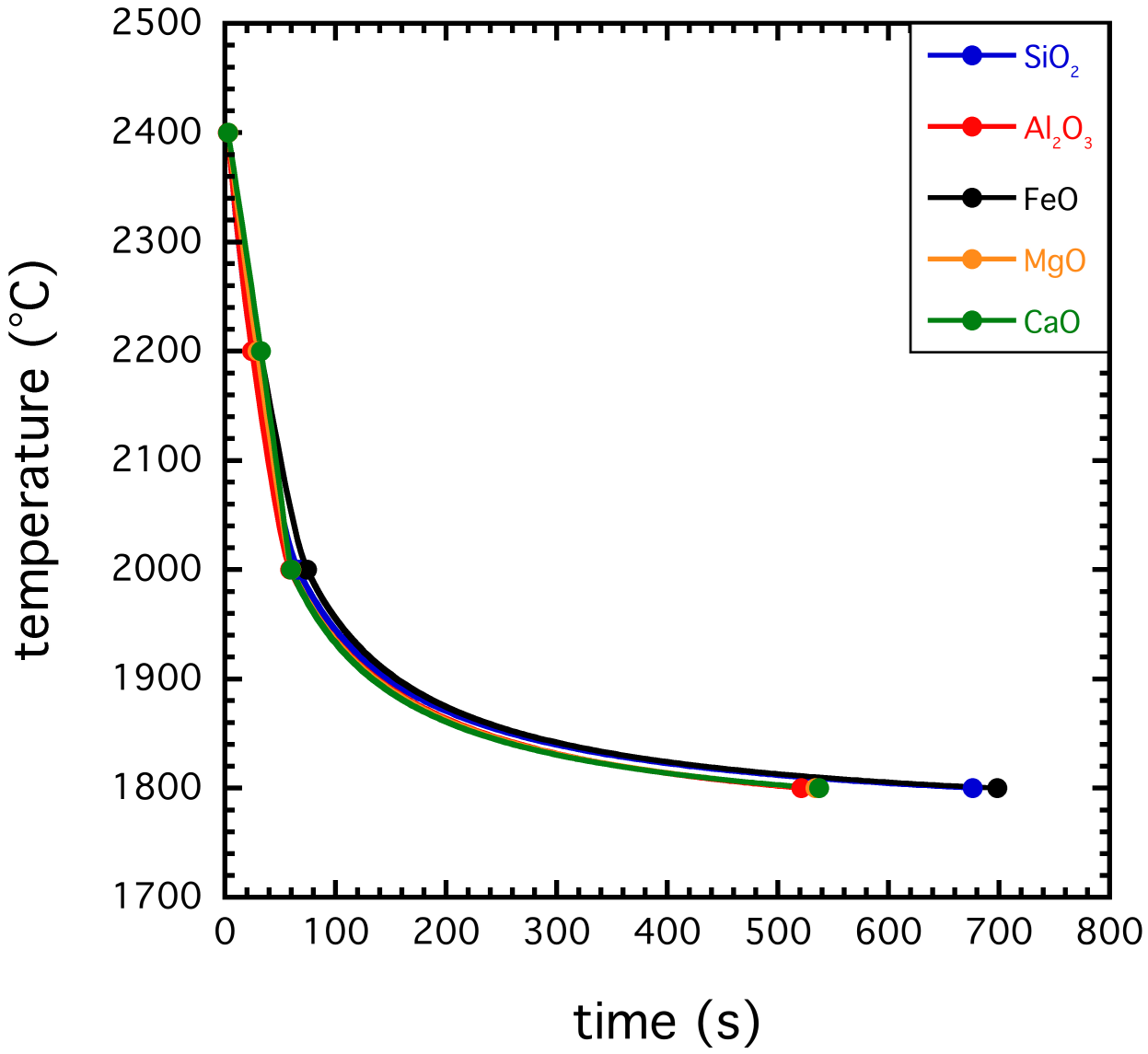

Fig. 18

Figure 19

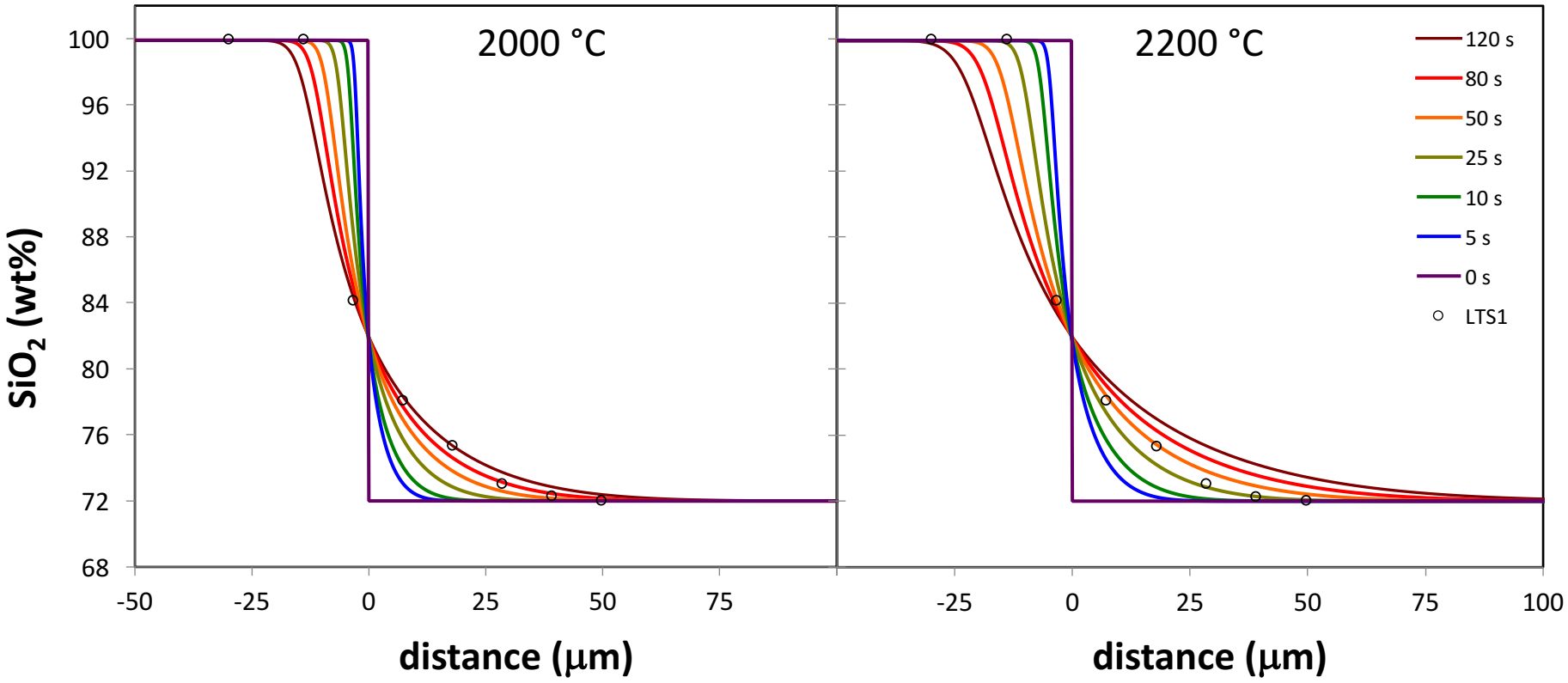

Fig. 19

Table 1 Average compositions (wt%) of felsic matrix glass and lechatelierite from tektite LTS1 and experimental starting materials (CIT-17640b and GRQ1) as determined by EMPA.

Oxide	LTS1 matrix[a]	2 SE[b] n=48[c]	LTS1 lechatelierite[d]	2 SE n=10	CIT-17640b[e]	2 SE n=24	GRQ1 quartz[f]	2 SE n=10
SiO_2	73.37	0.28	99.89	0.27	73.39	0.20	99.63	0.23
TiO_2	0.77	0.01	0.01	0.01	0.77	0.02	0.00	0.00
Al_2O_3	12.81	0.14	0.04	0.03	12.56	0.05	0.01	0.00
FeO	4.52	0.08	0.16	0.06	4.56	0.04	0.01	0.01
MgO	1.92	0.03	0.01	0.01	1.76	0.02	0.00	0.00
CaO	2.00	0.03	0.02	0.01	1.69	0.01	0.01	0.00
Na_2O	1.12	0.01	0.02	0.01	1.29	0.02	0.01	0.01
K_2O	2.30	0.01	0.05	0.03	2.58	0.01	0.00	0.00
Cr_2O_3	0.01	0.00	0.01	0.01	0.01	0.01	0.01	0.01
MnO	0.08	0.01	0.02	0.01	0.09	0.01	0.01	0.01
Total	98.92		100.22		98.71		99.68	

[a]Average oxide values of the matrix glass in indochinite tektite LTS1; data collected at least 200 μm away from any visible lechatelierite or schlieren.

[b]SE = standard error

[c]n = number of measurements

[d]Average oxide values of lechatelierite in indochinite tektite LTS1; data collected from center of lechatelierite.

[e]Average oxide values of matrix glass in indochinite tektite CIT-17640b (experimental starting material; data collected at least 200 μm away from any visible lechatelierite; no schlieren observed in this sample.

[f]Average oxide values of Hot Springs, AR quartz (experimental starting material).

Table 2 Heating temperatures and durations for levitation experiments. Diffusion profile lengths between lechatelierite and felsic matrix glass in experiments and natural tektite LTS1.

Sample name	*T* (°C)	time (s)	Diameter[a] (mm)	Profile name	Distance to edge[b] (μm)	Profile length[c] (μm)				
						SiO_2	Al_2O_3	FeO	MgO	CaO
Experiments[d]										
ALLF22	1800	1	1.8	22.1r	271	1.5	2.2	1.8	1.9	2.0
ALLF21	1800	5	1.9	21.2r	56	1.0	2.0	1.0	1.0	1.0
ALLF19	1800	10	1.7	19.2r	392	2.1	4.6	4.5	7.9	4.6
ALLF18	1800	25	1.7	18.1.2r	523	5.0	4.9	4.6	4.4	7.4
ALLF17	1800	50	1.7	17.1.1r	145	6.2	6.2	6.9	7.8	8.3
ALLF16	1800	80	2.2	16.1bl	807	5.5	7.6	7.7	7.8	7.6
				16.2r	321	6.2	5.6	5.7	6.6	5.6
ALLF8	2000	1	1.9	8.1br	822	2.9	3.5	3.9	4.3	3.6
				8.1bl	809	1.9	4.0	4.0	4.9	4.8
ALLF7	2000	5	1.6	7.1br	628	4.9	4.6	4.9	4.8	5.2
				7.1bl	650	6.0	6.3	7.0	7.4	7.2
ALLF6	2000	10	1.7	6.1br	733	8.4	8.4	8.4	7.5	8.0
ALLF5	2000	25	1.7	5.1br	175	13.1	13.9	15.6	18.0	17.0
				5.1bl	197	12.8	11.4	13.3	13.2	13.7
ALLF4	2000	50	2.0	4.1bl	585	17.0	17.3	20.8	20.4	21.1
				4.1br	646	15.7	14.9	16.3	18.8	16.3
ALLF3	2000	80	1.7	3.2bl	334	20.4	22.3	24.7	23.5	24.8
				3.2br	312	21.6	26.0	23.8	32.7	31.2
ALLF2	2000	120	1.5	2.1br	224	24.5	24.2	23.8	24.8	25.4
ALLF13	2200	1	2.2	13.1br	769	4.1	3.5	3.2	6.3	5.9
				13.1bl	763	5.2	7.8	7.7	8.1	8.0
ALLF12	2200	5	2.0	12.1br	725	8.8	7.2	9.4	11.0	10.4
				12.1bl	759	8.2	8.3	8.9	10.7	10.5
				12.2br	94	8.4	9.1	8.4	10.9	9.1
				12.2bl	106	9.6	11.6	9.3	8.8	9.2
ALLF11	2200	10	1.7	11.1br	866	18.9	19.6	19.6	20.9	21.7
				11.1bl	931	17.9	18.5	20.9	20.6	19.3
				11.2br	228	16.3	13.1	16.8	17.9	16.8
ALLF23	2200	50	1.9	23.1bl	658	22.5	22.5	23.1	23.5	21.8
				23.2br	650	21.7	22.7	22.0	26.1	25.4
				23.2bl	614	20.4	15.4	20.0	18.2	17.0
ALLF10	2200	80	2.2	10.1bl	859	33.7	29.4	33.2	34.2	31.6
				10.1br	1010	32.8	32.9	33.7	32.7	30.8
ALLF14	2200	120	2.3	14.1bl	221	47.3	51.9	46.7	51.8	50.2
				14.2bl	676	43.8	44.1	46.3	42.9	38.9
ALLF24	2400	1	2.0	24.1br	819	12.1	12.1	13.0	14.3	12.4
				24.3br	297	10.3	10.9	11.4	10.5	13.0

				24.3bl	300	11.3	11.8	13.2	12.3	11.9
Natural Sample										
LTS1	-	-	2030	7.1r	3219	21.3	20.2	24.1	23.6	22.3
	-	-	1920	2.1r	n.a.[e]	18.1	19.8	24.5	22.4	22.5
	-	-	1920	2.2l	n.a.	17.9	18.1	17.9	16.9	18.0
	-	-	2030	7.4.1l	3525	15.3	17.7	15.5	15.0	15.3
	-	-	2030	7.4.1r	3736	20.2	18.1	25.8	25.6	23.1
	-	-	2030	7.6r	222	22.9	20.3	25.3	27.8	25.6
	-	-	2030	7.4.2r	3746	18.0	17.9	22.0	21.1	24.2
				average		**19.1**	**18.9**	**22.2**	**21.8**	**21.6**
				1σ[f]		2.5	1.2	4.0	4.5	3.6

[a]Diameter of experimental glass spheres measured after heating. Diameter of natural sample indicates is measured along the longest dimension of the tektite's cross section.
[b]The distance from the profile to the nearest edge in experiments and in the natural sample.
[c]Errors for profile lengths are $\pm 1\mu m$ (1σ).
[d]Data presented for between 1-4 profiles in each experiment. Some profiles were compromised by proximity to vesicles, other lechatelierite, schlieren, shape of the lechatelierite beneath the polished surface, or polishing scratches on the surface, and are not included.
[e]n.a. = not available; the distances from the edge were not measured for these profiles
[f]Error for natural tektite LTS1 based on the standard deviation of 7 profiles in that sample.

Table 3 Activation energy (E_a) and pre-exponential factor (D_0) values determined from diffusion experiments in this study from 1800-2400 °C using Eqs. (2) and (4).

method[a]	diffusing component	melt composition[b]	ln D_0 (D_0 in m^2/s)	2σ[c]	E_a (kJ/mol)	2σ[c]
Eq. (2)[d]	SiO_2	intermediate	-7.13	2.19	399	11
	Al_2O_3	intermediate	-7.81	2.44	384	13
	FeO	intermediate	-7.37	2.67	391	13
	MgO	intermediate	-8.30	2.72	371	13
	CaO	intermediate	-8.36	3.08	370	14
Eq. (4)[e]	SiO_2	felsic	-6.46	1.69	392	8
		~pure silica	-9.46	1.69	392	8
	Al_2O_3	felsic	-8.20	1.21	356	6
		~pure silica	-12.17	1.90	343	9

[a]The diffusivities used to determine values of E_a and D_0 reported here were obtained using two different methods, Eqs. (2) and (4).

[b]The diffusivities in our experiments vary with varying composition along traverses across the lechatelierite-felsic glass boundary. Here we report values determined from diffusivities using Eq. (4) at points closest to the lechatelierite as '~pure silica,' and values determined at the end of a traverse in the felsic matrix as 'felsic.' Values determined from diffusivities obtained using Eq. (2) are thought to represent an average diffusivity along the profiles, and are reported here as 'intermediate.' See text for further explanation.

[c]Errors represent 2 standard deviations of the slope and y-intercept based on linear regressions of diffusivities on an Arrhenius diagram used to determine E_a and D_0, respectively.

[d]Eq. (2) was used to obtain diffusivities of all non-alkali oxides at 1800-2400 °C using the relationship between interdiffusion profile lengths and the square root of time. See §4.2.3 for complete discussion. The values presented here are calculated by fitting a line through these diffusivities on an Arrhenius diagram, where D_0 is the y-intercept, and the slope is used to solve for E_a.

[e]Eq. (4) was used to obtain diffusivities of SiO_2 and Al_2O_3 at 1800-2400 °C by assuming that the diffusivity of a component is exponentially dependent on its concentration. See §5.1.2 for complete discussion. The values presented here are calculated by fitting a line through these diffusivities on an Arrhenius diagram, where D_0 is the y-intercept, and the slope is used to solve for E_a.